DEPARTMENT OF PHYSICS
UNIVERSITY OF JYVÄSKYLÄ
RESEARCH REPORT No. 1/2014

PERIODIC NANOSTRUCTURES FOR THERMAL ENGINEERING APPLICATIONS

BY
TERO ISOTALO

Academic Dissertation
for the Degree of
Doctor of Philosophy

To be presented, by permission of the
Faculty of Mathematics and Science
of the University of Jyväskylä,
for public examination in Auditorium FYS1 of the
University of Jyväskylä on February 24, 2014
at 12 o'clock noon

Jyväskylä, Finland
February, 2014

Preface

The work presented in this thesis has been carried out at the Department of Physics and Nanoscience Center at the University of Jyväskylä.

First, I would like to thank my advisor, Professor Ilari Maasilta for the opportunity to work on such interesting projects and for his guidance and seemingly endless supply of ideas. Thanks to Dr. Panu Koppinen for teaching me his fabrication secrets and to Dr. Jenni Karvonen for inspiring a respect for proper cleanroom protocol. I thank Dr. Thomas Kühn, Dr. Jenni Andersin, Dr. Tuomas Puurtinen, Dr. Jussi Toppari and Dr. Andreas Johansson for many enjoyable and useful discussions. I would also like to thank Dr. Nobuyuki Zen for fruitful collaboration and friendship and Ms. Yaolan Tian for her hard work in assisting with and eventually taking over a demanding project. Many thanks to former and current group members, Dr. Lasse Taskinen, Dr. Minna Nevala, Dr. Kimmo Kinnunen, Dr. Saumyadip Chaudhuri, Mr. Mikko Palosaari, Mr. Juhani Julin, Mr. Zhuoran Geng and Mr. Andrii Torgovkin for collaborations and for sharing their wealth of knowledge. I thank Mr. Antti Nuottajärvi and Mr. Tarmo Suppula for their tireless efforts in keeping the labs and equipment in working order and all my colleagues at the Nanoscience Center for a wonderful working environment. From the Physics Department, I would like to thank both the administrative staff and the workshop staff for their dedication. Financial support from the National Graduate School in Nanoscience and the Academy of Finland is gratefully acknowledged.

Finally, I would like to extend my appreciation to family and friends for their encouragement during my studies, particularly my godparents, Juha and Eila Aspinen for their incredibly generous support throughout my time here and my father, Heikki Isotalo for his unwavering belief in my abilities.

Most of all, I am thankful to my beloved wife, Somjai for her love and understanding and to my wonderful children Aida and Nikko for their beautiful smiles which kept me in good spirits through tough times.

Jyväskylä, Spring 2014

Tero Isotalo

Abstract

Isotalo, Tero Jesse
Periodic Nanostructures for Thermal Engineering Applications
Jyväskylä: University of Jyväskylä, 2014
(Research report/Department of Physics, University of Jyväskylä,
ISSN 0075-465X; 1/2014)
ISBN 978-951-39-5611-0
diss.

This thesis is focused on periodic nanostructures and more specifically, the fabrication and characterization of two-dimensional (2D) and three-dimensional (3D) periodic nanostructures designed to produce phononic band gaps at sub-kelvin temperatures. Understanding and controlling thermal transport are of great interest from both a fundamental science perspective and an application perspective. While periodic nanostructures have been studied for their useful optical properties, comparatively little research has focused on the use of such structures for thermal engineering applications.

A method for producing 2D phononic crystals (PnCs) on suspended silicon nitride membranes is detailed in Chapter 2. This method includes the integration of superconducting tunnel junction devices within the PnC to function as thermometers and heat sources. Two square geometries, with lattice constants of 970 nm and 2425 nm, are investigated experimentally. The filling fraction of holes is fixed at 0.7 for both lattices. This gives a smallest feature size, at the narrowest point between holes, of 57 nm and 135 nm for the small and large lattice constant respectively. Thermal transport characteristics of these PnC membranes are compared to those of plain membranes at bath temperatures from 70 mK up to 1 K. An order of magnitude reduction in transmitted power is observed in the periodic structure compared to the unaltered membrane.

Dispersion relations, calculated by finite element method (FEM), of the various geometries under study are presented. Using the dispersion relations, the ballistic thermal conductances were calculated and found to be in excellent agreement with the experimental results. It was also found, both experimentally and theoretically, that a wider phonon band gap does not necessarily correspond to lower thermal

transport.

The fabrication of three-dimensional phononic crystals by vertical self-assembly (dipping method) of polystyrene (PS) nanospheres is described in Chapter 3. Colloidal crystals of 260 nm diameter PS nanospheres were produced on hydrophilic substrates and characterized by scanning electron microscopy. Statistical analysis of the size of continuous colloidal crystal domains revealed a trend in size distribution across all deposition parameters investigated. Domain sizes were found to exhibit a log-normal distribution, hinting at the dominant mechanism(s) controlling the self-assembly of the colloidal crystals.

Dispersion relations of the common 3D lattice structures produced by colloidal crystallization were also calculated by FEM. These calculations suggest that the width of the phonon band gap of these 3D phononic crystals can be tuned by varying the contact area between spheres. A highly controllable method for realizing this experimentally was demonstrated.

A method for fabricating tunnel junction devices on the surfaces of colloidal crystals is proposed in the final section of Chapter 3. Conducting metal wires of micrometer scale were successfully deposited on colloidal crystal surfaces at lengths of several tens of microns. Although yield was relatively low and conductivity still an issue, metal wires of sub-micron width were also successfully deposited. This opens up the possibility for constructing similar comparisons of thermal transport for 3D periodic nanostructures.

Chapter 4 briefly describes preliminary experiments on one-dimensional (1D) suspended nanostructures. Some of the operational principles and fabrication challenges common to all the experiments in this thesis are also introduced. Fabrication of nanoscale beams of silicon nitride (SiN) with superconducting tunnel junctions on top is detailed and their thermal transport properties investigated. Variations in device geometry and their effects on device performance are described. Electronic and phononic cooling of nanoscale beams using tunnel junctions is demonstrated and the potential of using boundary engineering to enhance the performance of such devices is presented.

Keywords Phononic Crystal, Self-assembly, Phonon Band Gap

Author's address Tero Jesse Isotalo
Department of Physics
Nanoscience Center
University of Jyväskylä
Finland

Supervisor Professor Ilari Maasilta
Department of Physics
Nanoscience Center
University of Jyväskylä
Finland

Reviewers Dr. Mikko Möttönen
Aalto University
Department of Applied Physics
Otaniemi
Finland

Dr. Jérôme Vasseur
University of Science and Technology Lille 1
Institute for Electronics, Microelectronics and Nanotechnology
Lille
France

Opponent Prof. Barry Zink
University of Denver
Department of Physics and Astronomy
Denver, Colorado
USA

List of Publications

The main results of this thesis have been reported in the following articles:

A.I. N. ZEN, T.A. PUURTINEN, T.J. ISOTALO, S. CHAUDHURI, AND I.J. MAASILTA, *Engineering thermal conductance using a two-dimensional phononic crystal*. Nature Communications *In Press*.

A.II. T.J. ISOTALO, Y.L. TIAN, M.P. KONTTINEN AND I.J. MAASILTA , *Statistical characterization of self-assembled colloidal crystals by single-step vertical deposition*. Colloid. Surface. A **443** (2014) 154-170.

A.III. T.J. ISOTALO, Y.L. TIAN AND I.J. MAASILTA, *Fabrication and Modelling of Three-Dimensional Sub-kelvin Phononic Crystals*. J. Phys.: Conf. Ser. **400** (2012) 052007.

A.IV. T.J. ISOTALO, Y.L. TIAN, M.P. KONTTINEN AND I.J. MAASILTA , *Tunable Solubility of Self-Assembled Colloidal Crystals by Electron Beam Exposure*. manuscript.

A.V. P.J. KOPPINEN, T.J. ISOTALO AND I.J. MAASILTA, *Boundary engineering for SINIS bolometers with integrated tunnel junction coolers*. AIP Conf. Proc. **1185** 318 (2009).

Author's contribution

The author of this thesis has written articles A.II and A.III. The author participated actively in writing A.I and A.IV. The author contributed to sample measurements for A.I and A.V. The data analysis in A.II and A.V was done by the author, and in A.III, the author is responsible for modeling and simulations. The author was responsible for significant sample fabrication for A.I, A.III, A.IV. and A.V.

Contents

List of Figures

Chapter 1

Introduction

1.1 Nanoscale materials and structures

Micro-electro-mechanical-systems (MEMS) and nano-electro-mechanical-systems (NEMS) are the basis for many of the devices we use every day. Computers, cellular phones and global positioning systems (GPS) all rely on MEMS devices at their cores. They can be as simple as a pressure sensor or an accelerometer or as complicated as bioMEMS lab-on-chip devices. As miniaturization has continued, the problem of excess heat in integrated circuits has become increasingly relevant. In the most ultra-sensitive detectors, reducing thermal noise is critical to improving performance. The precision of measurements and measurement devices is increasingly important as new technologies for both research and consumer products are developed. Even with fabrication challenges and device imperfections removed, sensitivity will eventually be limited by thermal fluctuations. Without proper thermal management, these devices will not function properly. Using cryogenic techniques to lower the operating temperature is one method to reduce thermal background noise. Thus, ultra-sensitive detectors are often operated at sub-kelvin temperatures. However, there are some applications in which current cooling techniques are either incompatible or do not reduce the thermal fluctuations enough. In such cases, the potential need for additional thermal isolation is great. As a result, understanding heat flow at the nano-scale is of particular interest in the development of modern MEMS/NEMS applications. In this work, we studied the effects of nanoscale structural design on phonon thermal transport at low temperatures, using superconducting tunnel junctions as thermometers.

1.2 Phonons

1.2.1 Phonons in Insulators

Phonons are the acoustic equivalent to photons. While a photon is a quantized vibration of the electromagnetic field, a phonon is a quantized vibration of a material lattice. The Debye theory begins with the assumption that lattice vibrations in a solid are caused by quantum oscillators [1]. These oscillators are characterized by and emit energy in quantized packets which are considered to behave like particles. Much like the photon is a particle representing an energy quantum of electromagnetic radiation, the phonon, as a particle, is an energy quantum of a lattice vibration. For insulators, phonons are the dominant source of thermal energy transfer and thus, energy transfer is determined by lattice vibrational states. At high temperatures, all possible vibrational states of the atoms are excited.

A given phonon wavevector $\mathbf{q}$ in a crystal of volume V has a corresponding q-space volume $(2\pi)^3/V$ [2]. The number of modes N_q of each polarization whose wavevector is smaller than q is then

$$N_q = \frac{V}{(2\pi)^3}\left(\frac{4\pi q^3}{3}\right) , \tag{1.1}$$

where $(4\pi q^3/3)$ is the volume of a sphere of radius q. The dispersion relation is assumed to be linear and defined by $\omega = v_s q$, where v_s is the average acoustic velocity defined by

$$\frac{1}{v_s^3} = \frac{1}{3}\left(\frac{1}{v_\ell^3} + \frac{1}{v_{t1}^3} + \frac{1}{v_{t2}^3}\right) . \tag{1.2}$$

where v_ℓ, v_{t1}, and v_{t2} are the longitudinal and the two transverse acoustic velocities respectively. The density of states given by $D(\omega) = \mathrm{d}N_q/\mathrm{d}\omega$ can then be written

$$D_m(\omega) = \begin{cases} \dfrac{3V}{2\pi^2 v_s^3}\omega^2 & \text{for } \omega \le \omega_D \\ 0 & \text{for } \omega > \omega_D \end{cases} , \tag{1.3}$$

where the maximum ω_D is called the Debye frequency and is defined by

$$\omega_D^3 = 6\pi^2 v_s^3 \frac{N}{V} , \tag{1.4}$$

where N is the total number of modes.

For a system of 3D vibrational normal modes indexed by $\mathbf{q}$ and m with occupation number $n_{\mathbf{q}m}$ and frequency $\omega_{\mathbf{q}m}$, the quantum mechanical total energy can be written

$$E_{tot} = \sum_{\mathbf{q}m} \left(n_{\mathbf{q}m} + \frac{1}{2} \right) \hbar\omega_{\mathbf{q}m} \ , \tag{1.5}$$

where $\mathbf{q}$ is the wave vector and m is the polarization of the mode. In contrast to photons, which have two possible transverse polarizations, phonons have an additional degree of freedom allowing longitudinal polarization. Continuing with the assumption that phonons behave as a collection of identical harmonic oscillators [2], we can describe the thermally averaged occupation number by the Bose-Einstein function

$$\langle n_{\mathbf{q}m} \rangle = \frac{1}{e^{\hbar\omega_{\mathbf{q}m}/k_B T} - 1} \ . \tag{1.6}$$

The average energy of the mode $\mathbf{q}m$ at a temperature T is then

$$\langle E_{\mathbf{q}m} \rangle = \left(\langle n_{\mathbf{q}m} \rangle + \frac{1}{2} \right) \hbar\omega_{\mathbf{q}m} \ , \tag{1.7}$$

and the total average energy will be given by summing the energies over all the phonon modes $\mathbf{q}$ and polarizations m as follows:

$$E_{tot} = \sum_{\mathbf{q}m} \left(\langle n_{\mathbf{q}m} \rangle + \frac{1}{2} \right) \hbar\omega_{\mathbf{q}m} = \sum_{\mathbf{q}m} \left(\frac{1}{e^{\hbar\omega_{\mathbf{q}m}/k_B T} - 1} + \frac{1}{2} \right) \hbar\omega_{\mathbf{q}m} \ . \tag{1.8}$$

In the equation above, it can be seen that the temperature-dependent contribution to total energy falls off exponentially. At low enough temperatures, this contribution vanishes leaving only the temperature-independent part or "zero-point" energy $\frac{1}{2}\hbar\omega$. This phenomenon is often referred to as the "freezing out" of higher temperature phonons.

1.2.2 Phonon Heat Capacity

Heat capacity at constant volume is defined

$$C_V = \left(\frac{\partial E_{tot}}{\partial T} \right)_V \ . \tag{1.9}$$

When the temperature is such that $k_B T/\hbar < \omega_D$ but still much larger than the frequency difference between modes, the sum over $\mathbf{q}$ in (1.8) can be replaced with an integral [2, 3]. Assuming the number of modes at a given polarization m to be $D_m(\omega)$, the total energy, neglecting zero point energy, can then be approximated by

$$E_{tot} = \sum_m \int D_m(\omega) \, \frac{\hbar\omega_m}{e^{\hbar\omega/k_B T} - 1} \, \mathrm{d}\omega \; . \tag{1.10}$$

Taking the derivative with respect to temperature T, we get the heat capacity for the lattice.

$$C_{\text{lat}} = \left(\frac{\partial E_{tot}}{\partial T}\right)_V = k_B \int D_p(\omega) \left(\frac{\hbar\omega}{k_B T}\right)^2 \frac{e^{\hbar\omega/k_B T}}{\left(e^{\hbar\omega/k_B T} - 1\right)^2} \, \mathrm{d}\omega \tag{1.11}$$

It should be noted here that there exists a lower limiting temperature for the integral approximation in (1.10) which depends on the solid dimensions. In a 1 mm^3 solid, the limit is 0.2 mK and in a 10 µm^3 solid it is as high as 20 mK [3]. This means that for nano-scale structures at very low temperatures, the approximation breaks down. The insulating solids in the preliminary measurements of this study are on the order of 0.03 mm^3 and thus fall well within the approximation boundaries. In the case of very thin suspended bridges however, this effect needs to be taken into account.

1.2.3 Thermal Resistivity

Scattering from crystal boundaries or impurities and phonon-phonon interactions determine the mean free path l of phonons and thus the thermal resistivity of the phonon gas. The Debye temperature θ_D defines important ranges for the phonon interactions and is defined by [2]

$$\theta_D = \frac{\hbar\omega_D}{k_B} \; . \tag{1.12}$$

Intermediate temperatures $T \geq \theta_D/10$ are dominated by phonon-phonon interactions [4]. Decreasing temperatures reduce the number of phonon modes and thus increases the phonon mean free path. Typical temperatures in this study are lower still and thus, a rigorous treatment is omitted here. A thorough discussion of thermal conductivity in this regime can be found in the literature [3]. At much lower temperatures $T \ll \theta_D/10$, the number of phonons is small enough that phonon-phonon scattering can be neglected. Crystal boundaries and defects become the primary scattering agents. The dominant phonon wavelength at these temperatures is typically larger than the size of lattice impurities [4], thus further restricting the scattering to lattice boundaries.

1.3 Tunnel Junctions

While tunneling is a familiar quantum mechanical phenomenon, the properties of superconductors make their use in tunnel junctions of particular interest and utility. In 1960, Ivar Giaever observed electron tunneling in a Normal metal-Insulator-Superconductor (NIS) junction. Subsequent experiments with such tunnel junctions verified the Bardeen-Cooper-Schrieffer (BCS) theory of superconductivity and in 1973, Giaever shared the Nobel prize in physics with Brian Josephson and Leo Esaki. Since then, the technology of NIS junctions has changed relatively little.

1.3.1 Tunneling

The tunnel barrier is commonly approximated by a rectangular potential between two conducting materials. In the case of NIS junctions, the tunneling behavior can be visualized as shown in Figure 1.1 below.

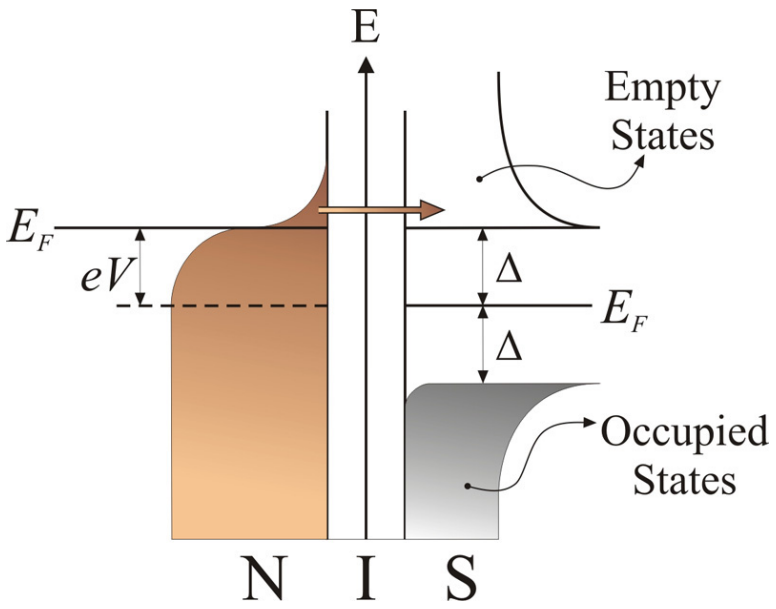

Figure 1.1: An energy diagram for a NIS junction shows "hot" electrons in the Fermi tail of the normal metal excited to energies just above the superconducting gap, allowing them to tunnel through the insulator into the unoccupied states in the superconductor.

When a voltage lower than Δ/e is applied over the junction, only the electrons in the tail of the Fermi distribution of the normal metal reach above the superconducting energy gap, and current then depends exponentially on the voltage. At voltages above Δ/e, electrons below E_F are also able to tunnel through the insulator into the superconductor, resulting in linear current-voltage characteristics.

1.3.2 NIS Junctions

The SINIS structure consists of two symmetric NIS junctions in series and as such, can be understood by inspecting the behavior of a single NIS junction with half the applied voltage. The I-V characteristics of a NIS junction are somewhat similar to those of a diode [5]. At voltages near the edge of the superconducting gap Δ, there is a sharp increase in current which then assumes the familiar linear I-V form of a resistor at significantly larger voltages. Ideally, the density of states (DOS) in the superconductor $N_s(E)$ is zero for quasi-electrons of energy E less than Δ. Above the gap, DOS is given by [6]

$$N_S(E) = N_N(E)\frac{|E|}{\sqrt{E^2-\Delta^2}} \ , \tag{1.13}$$

where $N_N(E)$ is the DOS in the normal metal. Assuming the DOS in the normal metal to be constant near the Fermi energy, the tunneling current can be written [6,7]

$$I(V) = \frac{1}{eR_T}\int_\Delta^\infty \frac{|E|}{\sqrt{E^2-\Delta^2}}[f(E-eV,T_e) - f(E+eV,T_e)]\mathrm{d}E \ , \tag{1.14}$$

where R_T is the tunneling resistance, e is the electron charge, and T_e is the temperature of electrons in the normal metal. It is worth noting that the current in the NIS junction does not depend on the temperature of the superconductor, but is very sensitive to the temperature of the normal metal, as will be shown in Figure 1.3. By applying a current bias through the junction, one can measure the voltage V, which is proportional to temperature. In practice, we calibrate the junction by measuring V as a function of the bath temperature. A typical measured V-T curve is shown in Figure 1.2.

The deviation of the experimental data from BCS theory seen in Figure 1.2 at low temperatures is indicative of the noise inherent in the setup. This is largely a consequence of the small size of the tunnel junctions. Noise heating leads to saturation of the junction temperature due to the strong decoupling of the electronic system from the lattice at low temperatures. Part of the deviation can also be attributed to a small but non-zero density of states within the gap [8], which may also be caused by external noise [9]. At $T_e = 0$, tunneling current would ideally be zero for voltages below the superconducting gap as the DOS in the superconductor is zero in this region. Above Δ/e, the tunneling current is then approximated by

$$I(V) = \frac{\sqrt{V^2-(\Delta/e)^2}}{R_T} \ . \tag{1.15}$$

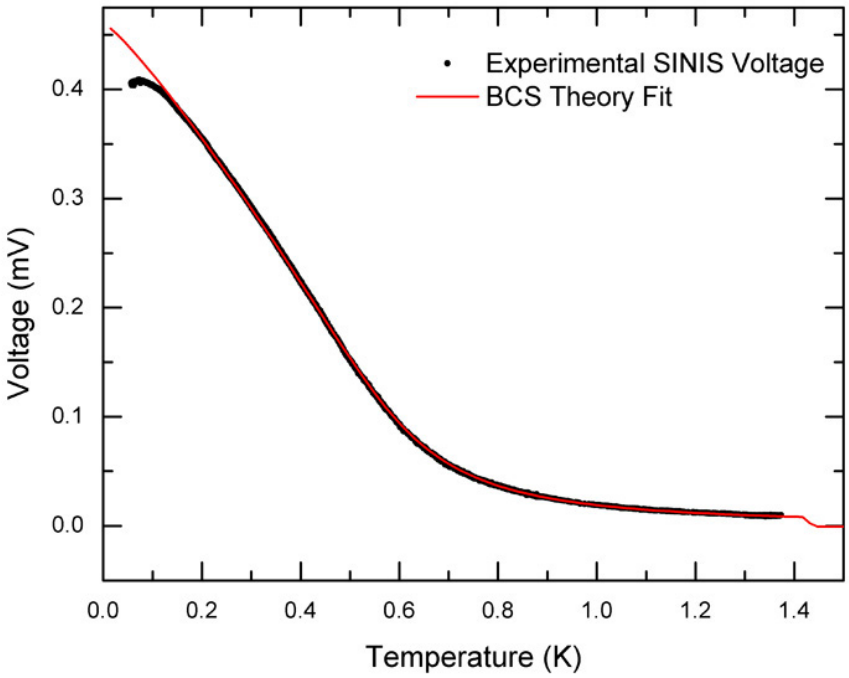

Figure 1.2: Voltage is measured across a SINIS structure at varying temperatures with a fixed current bias. The red curve is a fit of the BCS theory used in calibrating the SINIS.

As temperature T_e increases, the region in which the diode-like upturn in current takes place becomes more rounded. This limits the temperature range in which the SINIS thermometer is operable to $T_e \leq T_c$, where T_c is the critical temperature of the superconductor. Also limiting the performance of a SINIS thermometer is the thermal relaxation time τ of the sensing element (normal metal), in most cases given by

$$\tau = \left(\frac{\partial \dot{Q}_{e-ph}}{\partial T_e} \right)^{-1} C_e \ , \tag{1.16}$$

where $\dot{Q}_{e-ph} = \Sigma\Omega(T_e^5 - T_{ph}^5)$ is the heat current between electrons and phonons for thick (t >30 nm) metal films [10] with Σ and Ω being the electron-phonon interaction constant and normal metal volume respectively and $C_e = \Omega\gamma T_e$ is the electronic heat capacity, with γ being the so-called Sommerfeld constant [7]. In some cases, other heat flow mechanisms, such as phononic or photonic thermal conductance dominate [11, 12] Substituting the expressions for heat current and electronic heat capacity into (1.16), we arrive at the following:

$$\tau = \frac{\gamma}{5\Sigma} T_e^{-3} \ . \tag{1.17}$$

Thus, we see that the response time of a SINIS thermometer is independent of the volume of the normal metal island. It depends on temperature and materially on the average electron-phonon scattering rate [7]. Such SINIS structures have been used successfully as sub-kelvin thermometers [13] and to directly measure the above mentioned electron-phonon relaxation rate in thin copper films [14].

1.3.3 SINIS Thermometer

Figure 1.3 below shows typical measured current-voltage characteristics of a pair of NIS junctions in series at different temperatures. Using such a set of I-V curves, one can select appropriate bias current I_b to apply to the device such that a change in temperature will result in a large, measurable change in voltage. However, it can be seen in the plot that one value of I_b does not suffice to cover the whole temperature range. Indeed, the two dashed horizontal lines in Figure 1.3 marked as 3.4 pA and 170 pA represent the bias currents used for thermometry at low and high temperature regimes respectively.

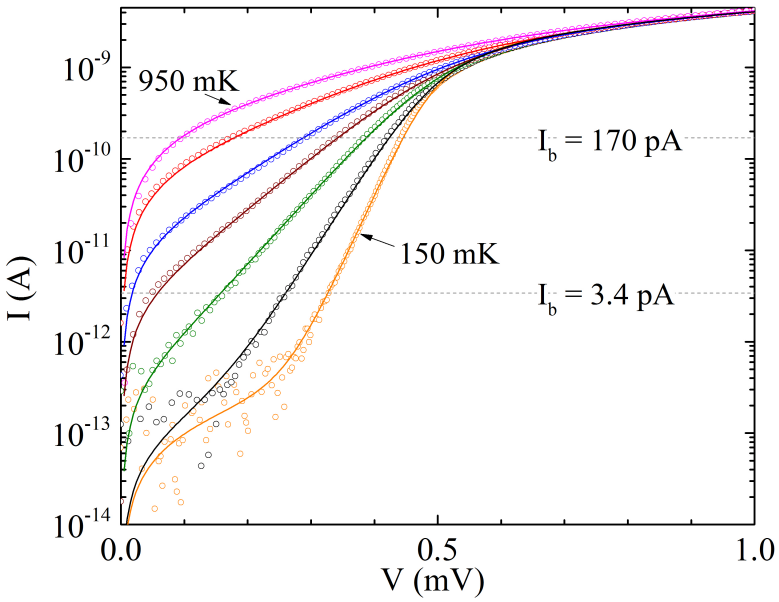

Figure 1.3: I-V characteristics for a SINIS thermometer measured at several bath temperatures. The two dashed horizontal lines at 3.4 pA and 170 pA represent the bias currents used for thermometry in the low and high temperature regimes respectively.

1.3.4 Electronic and Phononic Cooling By Tunnel Junctions

The basic principle of cooling of a NIS tunnel junction is based on the existence of the superconducting energy gap Δ for single particle electronic excitations (Figure 1.1). An electron from the normal metal can only enter the superconductor if it has at least energy Δ. At finite temperatures, electrons typically follow the Fermi-Dirac distribution and thus, even at biases $eV < \Delta$ there are some energetic electrons that can tunnel through the insulating barrier. These hot electrons take energy with them, lowering the temperature of the remaining electrons in the normal metal. See Section 4.3 and [11] for a more detailed discussion of tunnel junction cooling.

1.4 Basic Fabrication Methods

1.4.1 Membrane Sample Preparation

Sample fabrication for the 1D and 2D structures begins with a silicon (Si) wafer 300 μm thick coated on both sides with silicon nitride typically of 750 nm or 300 nm thickness obtained from the University of California at Berkeley. Sections were cut from the center of the wafer to ensure consistency of the nitride films. In some cases we desired a thickness of the membrane different from the prefabricated thickness. In such cases, one side of the section was thinned by reactive ion etching (RIE) using an Oxford Instruments Plasmalab 80 system to get the desired thickness. CHF_3 plasma etch was performed at 50 mTorr pressure for 8 minutes using a 13.7 MHz source at 150 W power. Flow rates of CHF_3 and O_2 were kept at 50 and 5 sccm respectively, resulting in an etch rate of approximately 26 nm/min. Starting temperature in the chamber was between 27 and 30 °C and increased during the etch by a maximum of 4 degrees. The slow rate of etch ensures a low surface roughness and more precise control of the final film thickness. Next, individual sample chips measuring 8×8 mm were cut from the wafer section. Alternatively, individual chips can be cut first and then thinned by the above procedure. This technique however, often results in an uneven etch profile due to edge effects. Such edge effects seem to be enhanced when multiple chips are placed close to each other within the plasma chamber.

1.4.2 Membrane Fabrication

Membrane fabrication involves four basic steps as shown in Figure 1.4. The reverse side of these chips was prepared for bulk etching of the silicon to produce the suspended membrane as described below.

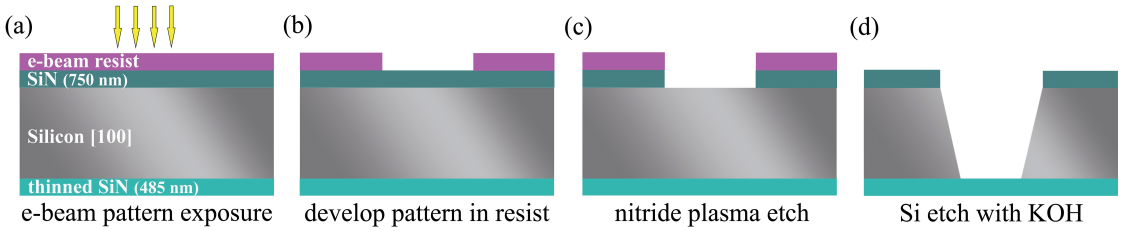

Figure 1.4: Lithography process steps are shown. (a) Pattern is exposed in electron-beam resist (PMMA), (b) resist pattern is developed, (c) SiN_x is etched with CHF_3 plasma and then (d) the Si substrate is etched anisotropically with KOH.

First, they were coated with two layers of polymethyl methacrylate (PMMA) in anisole with 7% concentration by weight. Each layer was deposited by spin coating at 3500 rpm for 60 seconds followed by 3 minutes baking at 160 °C. Total thickness for the two layers was 800 nm. Electron beam exposure was then performed using a Raith e-LiNE system with 20 kV accelerating voltage to pattern squares with lateral size approximately 700 μm in the resist. The pattern was developed in a 1:2 solution of methyl-isobutyl ketone (MIBK) and isopropanol (IPA) for 50 seconds, then rinsed in IPA for 30 seconds and dried under nitrogen gas flow. Nitride was etched using RIE with a plasma excitation power of 200 W with other parameters unchanged from the thinning etch. Remaining resist was removed in a hot acetone bath and rinsed in IPA. Silicon was then etched in potassium hydroxide (KOH) at 90 °C for approximately 6 hours to ensure the full 300 micrometers of Si was etched, producing a clean nitride membrane. Following the KOH bath, chips were rinsed 4 – 5 times in warm deionized water and finally in IPA and dried under nitrogen flow. At this point, the chips were ready for the fabrication of measurement circuitry.

1.4.3 Junction Fabrication

One layer of 9% PMMA in ethyl lactate was spin coated at 4000 rpm and a second layer of 4% PMMA in anisole was spin coated at 2250 rpm. Spin time, baking temperature and time for both were 60 seconds, 160 °C and 3 minutes respectively. Patterns were exposed in the resist using the Raith e-LiNE with 20 kV accelerating voltage. The smallest features were patterned using a 30 μm aperture, while the larger features (including bonding pads) were patterned with a 120 μm aperture. Using the larger aperture reduces the total patterning time considerably, but requires alignment of the two patterns in order to produce reliable electrical contacts in the final structure. Patterns were developed first with the 1:2 MIBK:IPA solution for 50 seconds, then rinsed with IPA for 30 seconds and dried under

nitrogen flow. An undercut pattern was achieved using a second developer consisting of 2-methoxyethanol and methanol (1:2) for 4 seconds, which was rinsed in IPA for 30 seconds and dried under nitrogen gas. Immediately following development, the sample was placed in the RIE chamber and pumped to system pressure. Residual resist within the developed pattern was removed with a room temperature O_2 plasma treatment using 60 W excitation power, 55 mTorr pressure for 30 seconds. The sample was then placed in the evaporation chamber for metal deposition.

Junctions were made with Aluminum (Al) as the superconductor and either Copper (Cu) or a double layer consisting of Cu and Gold (Au) serving as the normal metal. The thin Au layer protects the Cu from degradation during later processing as described in Section 4.1. Metals were deposited in an ultra-high vacuum (UHV) chamber at approximately 10^{-8} mbar using the electron-beam evaporation method. The Al was deposited from angles of ± 65 degrees to produce the superconducting wires for both the thermometer and heater as shown in Figure 1.5.

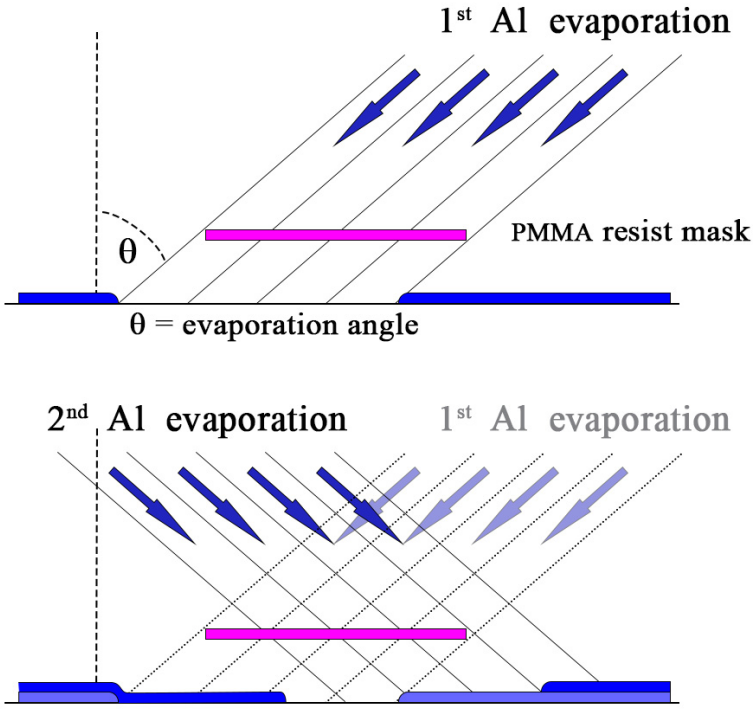

Figure 1.5: Aluminum wires are evaporated from 65 degree angles on both sides of the normal to produce the superconducting leads for thermometer and heater junctions.

Following the Al deposition, the sample chip was moved to the UHV loading chamber, where it was exposed to an oxygen atmosphere at 40 mbar for 4 minutes,

producing an aluminum oxide (AlO_x) layer on the Al wires. The sample chip was then rotated by 90 degrees within the loading chamber and moved back to the evaporation chamber. Using a similar two-angle evaporation technique, with ± 60 degrees, Cu and then Au were deposited. This angled evaporation, along with the narrow width of other patterned lines, avoided depositing normal metal on top of the superconducting leads near the center of the membrane. In this case, the two-angle technique also ensures proper coverage and electrical contact through the Cu wire by filling in the gaps left by shadowing of the Al wire, as shown in Figure 1.6.

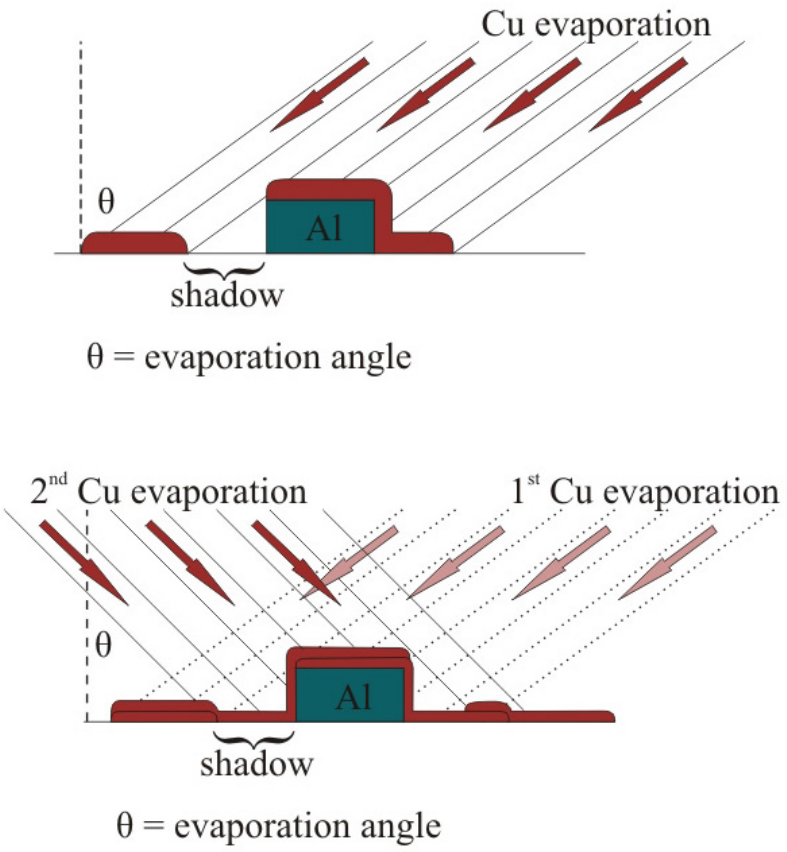

Figure 1.6: Proper electrical contact through the Cu over the oxidized Al wires was ensured by two-angle evaporation to fill in the gaps left by shadowing of the Al wire.

After deposition, the sample chip was removed from the UHV chamber and immersed in hot acetone for lift-off. The chip was then rinsed in IPA and dried under nitrogen flow. A false color SEM image of the final thermometer structure on a suspended SiN membrane is shown in Figure 1.7 below. The red and blue colored wires are the Cu normal metal and Al superconductor respectively.

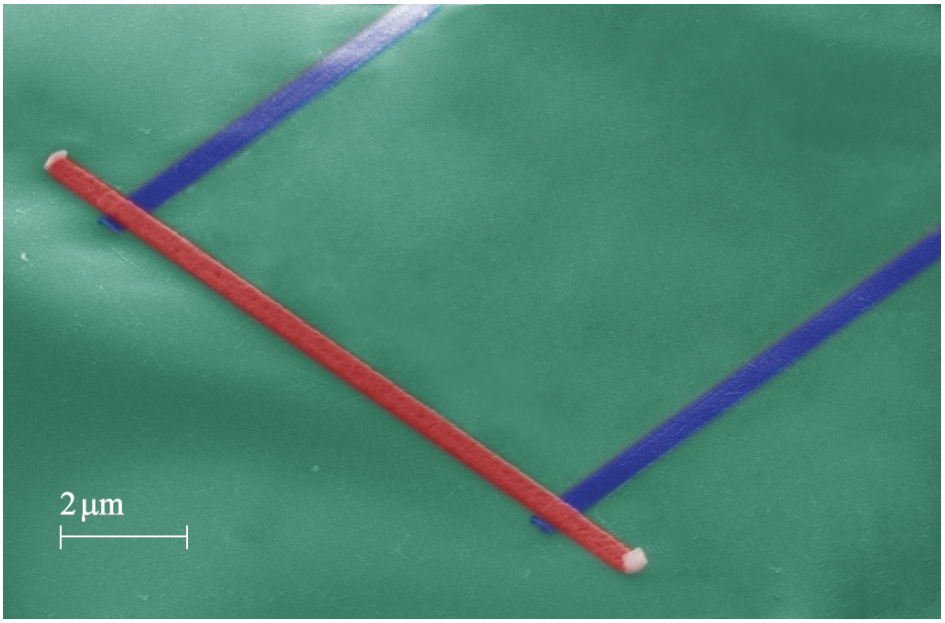

Figure 1.7: False color SEM image of the final thermometer junction structure is shown. Red and blue colors indicate the Cu normal metal and Al superconductor respectively. The whole structure is on a suspended SiN membrane.

1.4.4 Colloidal Crystallization

Fabrication of 3D phononic crystals (PnCs) begins with a substrate similar to the 2D samples. Two different types of 3D sample types were produced for these experiments. The simplest sample type consists of self-assembled polystyrene nanospheres deposited on a featureless substrate surface. The more complicated samples used lithographically patterned features on the substrate surface to direct the self-assembly of the nanospheres.

1.4.5 Colloidal Self-Assembly by Vertical Deposition

For the simple samples, a double-sided SiN_x chip was coated on one side with a hydrophilic titanium oxide (TiO_x) layer [15]. A 10 nm layer of titanium was electron-beam evaporated in an ultra-high vacuum (UHV) chamber at approximately 10^{-7} mbar pressure, then exposed to an oxygen environment at 100 mbar for 5 minutes. Polystyrene (PS) spheres of 260 nm diameter were deposited on the hydrophilic surface using vertical deposition [16].

Samples were held vertically and lowered into the PS sphere solution to a depth of approximately 10 mm. The arm was then raised slowly by control software to withdraw the sample from the solution. A schematic of the dipping method is shown in Figure 1.8 below.

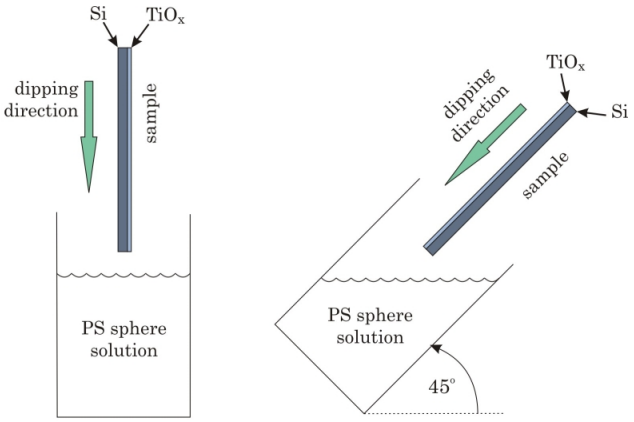

Figure 1.8: Schematics of the dipping setups are shown. TiO_x coated substrates were dipped either vertically or at a 45° angle.

The samples were held in place at the bottom of a movable dipping arm by a sample holder as seen in Figure 1.9. This apparatus is a modified Langmuir-Blodgett thin film coating device from KSV Instruments. The original vertical actuation motor has been replaced in order to achieve slower dipping speeds and the entire vertical motion mechanics have been separated from the original device to facilitate angled dipping. Also seen in Figure 1.9 is a typical PS sphere solution container into which the samples were submerged. It is well known that self-assembly by vertical deposition, like evaporative deposition, is dominated by fluid dynamics at the meniscus [17–20]. Consistent with that, we also determined that the speed of withdrawal from the solution was the dominant factor in self-assembly and thus, a higher speed could be used for submersion in order to reduce total dipping time. In addition to vertical dipping, some experiments were performed at a 45° angle for select combinations of dipping speed and solution concentration. Withdrawal speeds between 0.01 mm/min and 0.05 mm/min were investigated.

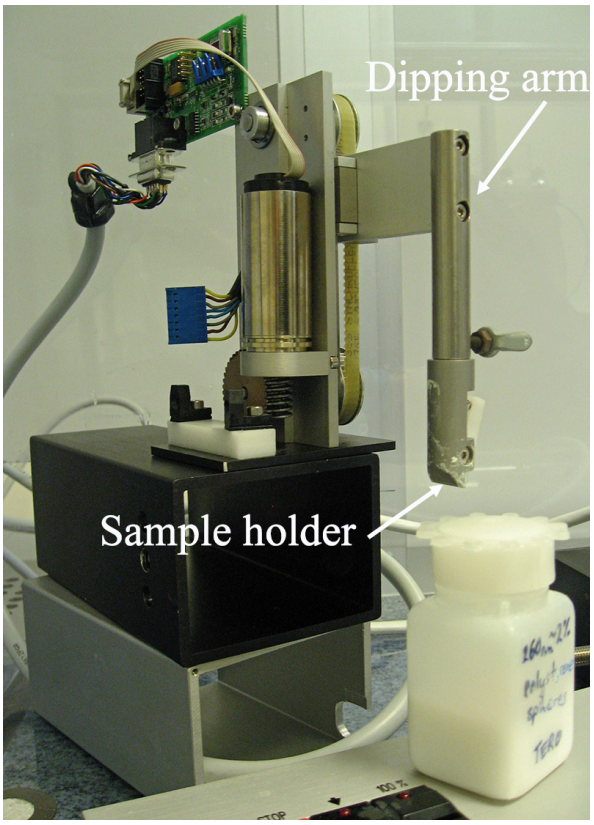

Figure 1.9: Modified Langmuir-Blodgett coating device used for vertical deposition is shown. The vertical movement of the dipping arm is controlled by a software interface.

Chapter 2

2D Periodic Structures

This chapter details the fabrication and characterization of 2D PnCs. A sample device consists of a suspended membrane with a superconducting tunnel junction thermometer and heater, surrounded by an array of holes etched through the membrane. Junctions are made up of two symmetric NIS devices, forming a SINIS configuration. Fabrication challenges as well as theoretical operation are addressed, followed by a summary of results.

2.1 2D Sample Fabrication

The protocol for producing 2D samples consists of four main processes – thinning, membrane release, junction fabrication and hole etching. First, a section of a double-sided silicon nitride SiN wafer was thinned on one side from 750 nm to 485 nm by reactive ion etching (RIE) in an Oxford Instruments Plasmalab 80 system, as described in Section 1.4.1. The other side nitride was then patterned by electron beam lithography (EBL) and etched by RIE to produce square openings of approximately 700 μm, as described in Section 1.4.2. The patterned nitride served as a mask for KOH wet etching of silicon, forming suspended membranes of SiN. Subsequently, EBL was used to expose a double-layer resist with the measurement device pattern on the membranes and multi-angle UHV evaporation was used to deposit metals for the devices (see Section 1.4.3). The combination of copolymer and PMMA resists ensures an undercut in the pattern which is critical to successful lift-off after metal evaporation.

2.1.1 Membrane Perforation

The final stage of sample fabrication for 2D PnC samples is to etch an array of holes to surround the heater and thermometer junctions. Two methods are detailed here

which both address the difficulties with Cu metal wires as described in Section 4.1. Replacing Cu completely with Au avoids the degradation from processing, however simply adding a thin Au coating of ∼10 nm, as described in Section 1.4.3, is also enough to protect the Cu wire from degradation. The first method described involved samples made with Au coated Cu wires. Two layers of 7% PMMA in anisole were spin coated at 3500 rpm and baked at 160 °C for 3 minutes each, resulting in a total PMMA thickness of 800 nm. A 6 nm layer of Al was then evaporated onto the resist layers in a UHV chamber. This acted as a conducting layer to reduce charging effects during patterning. The hole array pattern was exposed onto the resist with the Raith e-LiNE electron beam writing tool using 20 kV accelerating voltage and the Al layer removed by wet chemical etching in sodium hydroxide (NaOH) for 30 seconds. The pattern is then developed in 1:2 MIBK:IPA solution for 50 seconds, rinsed with IPA for 30 seconds and dried under nitrogen flow. Without the Al layer, patterns produced were consistently distorted. As this distortion was not seen in the patterning of junctions or hole arrays patterned on bulk (non-suspended) SiN, it seems likely that the high concentration of electron beam exposure in the center of the membrane lead to a buildup of charge which could not easily escape the highly insulating structure, resulting in beam deflection, and possibly resist re-flow. Adding the thin conducting layer allowed distortion free patterns to be consistently produced on suspended membranes. After development, samples were immediately placed in the RIE chamber and pumped to low pressure to minimize the exposure of moisture to the patterned resist. Additonally, a 30-second O_2 flash at 60 W removed any PMMA residue from the developed pattern. Holes were then etched through the SiN using a CHF_3/O_2 plasma with 100 W power and 55 mTorr pressure. Here, CHF_3 and O_2 flow rates were 50 and 5 sccm respectively. Etch time was 28 minutes, during which the chamber temperature increased approximately 7 degrees from 27 °C to 34 °C.

For samples using Cu alone as the normal metal, the following method was found to be a viable alternative. One layer of 7% PMMA in anisole was spin coated at 3500 rpm and dried by rough pumping for approximately one minute. A second layer of 7% PMMA in anisole was spin coated at 3500 rpm and dried similarly. This successfully removes the anisole solvent from the PMMA without using heat, which has been determined to damage Cu wires. Finally, the resist layers were baked for 3 minutes at 160 °C, after which the samples can be processed as usual without damaging the Cu wires underneath.

Figure 2.1 shows a false-color SEM image of a suspended SiN membrane with measurement devices and PnC structure. The suspended membrane area is seen as a large darkened square, while the smaller dark square in the middle is the array of

holes etched through the membrane.

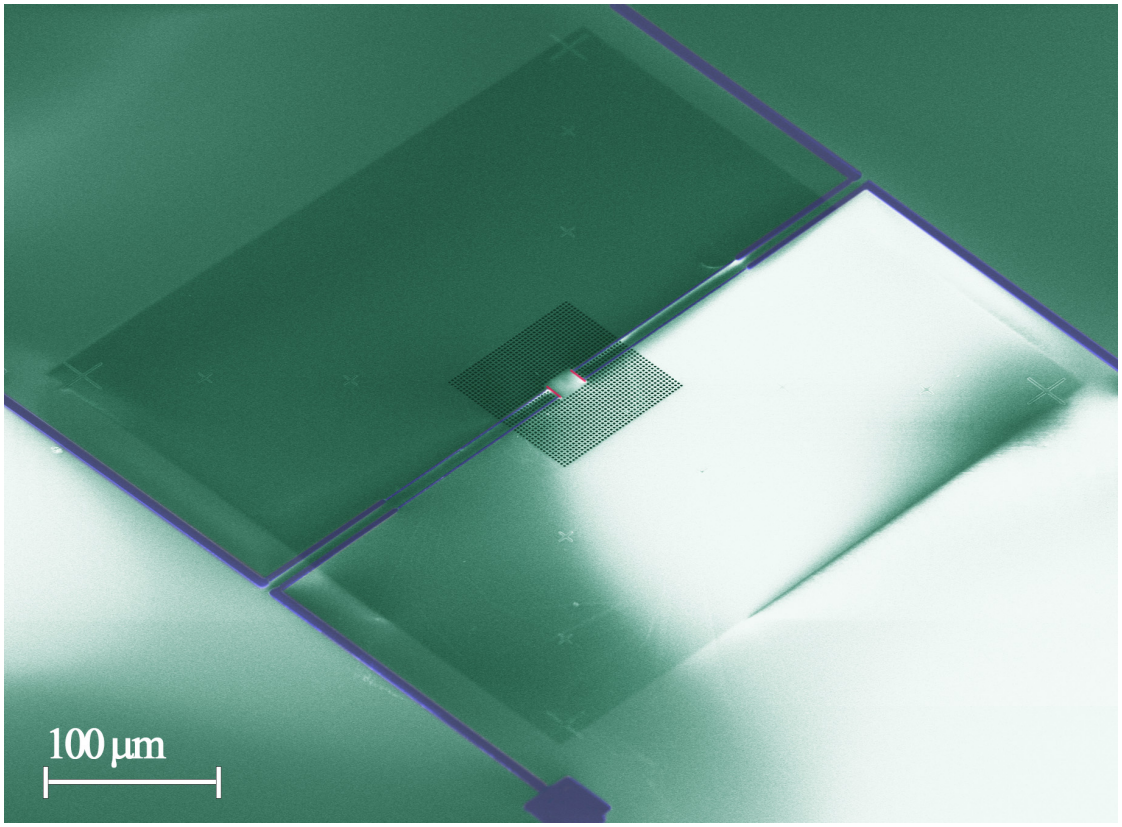

Figure 2.1: A 2D PnC sample is shown in a false color SEM image. The blue lines are aluminum superconducting wires and the red lines are copper normal metal wires forming the SINIS tunnel junction devices. Surrounding the junctions is an array of holes (dark inner square) with 2.3 µm diameter. The whole structure is fabricated on a suspended membrane (dark outer square) of SiN 485 nm thick.

2.1.2 Sample Specifications

Membranes of SiN 485 nm thick were used for all the 2D samples discussed in this work. Deposition of metals for tunnel junction devices and etching of the hole arrays were performed separately for each chip.

Four devices, three identical PnC devices and one plain membrane device, were fabricated on each chip. The membranes were squares of approximately 250 µm on a side, separated by 2.2 mm from each other on the chip. Figure 2.2 shows a false color SEM image of a PnC sample device with a close-up view of the SINIS junction pairs in the inset. Superconducting Al wires are shown in blue, while the Cu normal metal wires are shown in red. Line widths are kept narrow on the membrane and multi-angle deposition is used for both Al and Cu wires. In this

way, we ensure depositing only superconducting contacts from the center of the device to the bulk, further reducing pathways of electronic heat conduction.

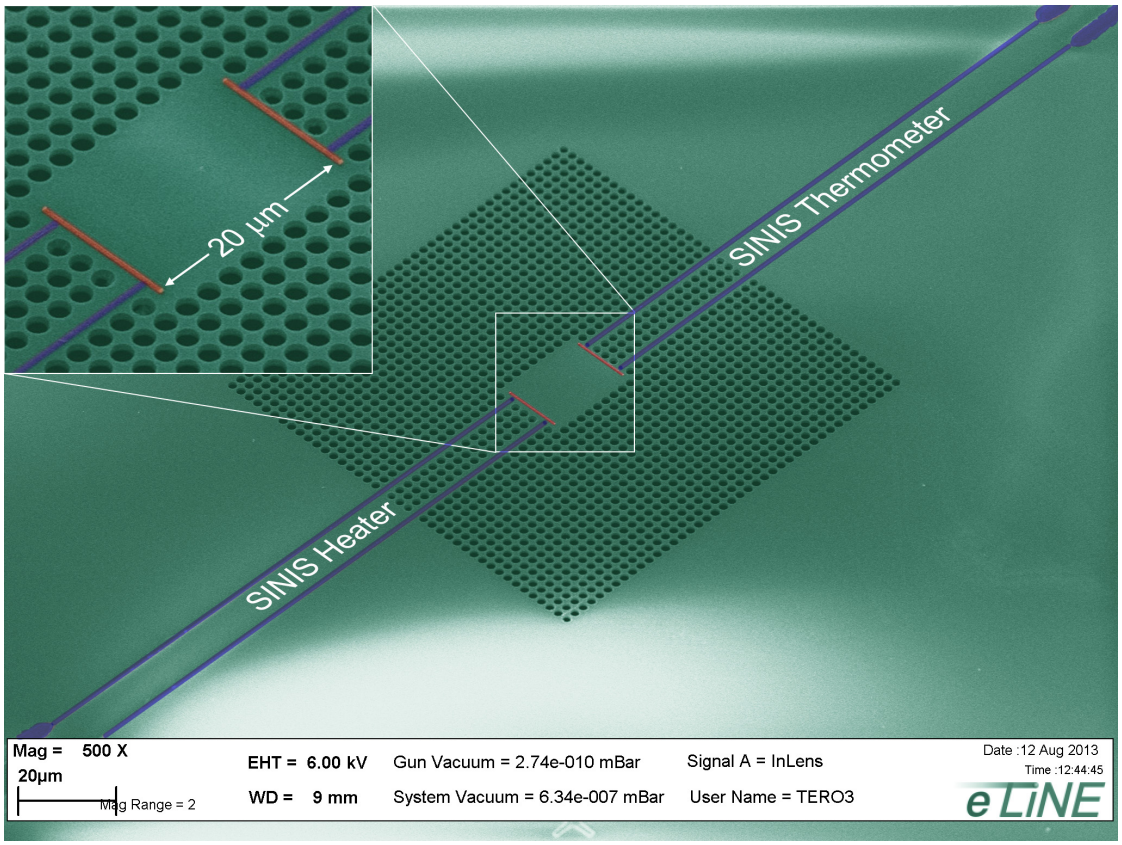

Figure 2.2: 2D PnC sample is shown in completed form. The diameter of holes is 2.29 µm while the lattice spacing is 2.425 µm, making the narrowest part between holes only 135 nm wide. The inset shows a closer view of the SINIS junction pairs.

The Al wires were oxidized at 40 mbar for 4 minutes to produce tunnel junctions with room temperature tunneling resistance R_T ranging from 15 – 30 kΩ. These resistances were checked just after lift-off, immediately following the etching of holes and after attaching to the cryostat sample stage to track the behavior of junctions throughout sample processing. Resistances increased approximately 10 – 20 kΩ between initial and final room temperature measurements.

2.2 Theory for 2D Phononic Crystals

2.2.1 Thermal Transport on Membranes

A silicon nitride (SiN) membrane is one of the most common substrates for ultra-sensitive bolometers and calorimeters [21]. As one lowers the temperature,

scattering of phonons is reduced such that thermal transport becomes predominantly ballistic [22–24].

2.2.2 2D Acoustic Bandgap

This section details the application of coherent band-structure effects in controlling phonon thermal conductance, using periodically nanostructured suspended membranes. We perforated SiN membranes with square arrays of circular holes, producing 2D PnCs. Two lattice constants were investigated here. One was selected to exhibit a maximum phononic bandgap for the dominant thermal phonons at 0.1 K, while the other was selected to have the same filling fraction with larger dimensions and no bandgap.

2.3 2D Results

The geometries of the PnC samples were selected with the help of numerical calculations of the phonon band structure. Finite element method (FEM) was used to solve the 3D elasticity equations for an isotropic material with periodic Bloch-wave boundary conditions for in-plane displacements. Values of the 2D wavevector k were varied within the first octant of the Brillouin zone (BZ) of a square lattice, as shown in Figure 2.3b.

Symmetry of the lattice gives solutions to the remaining octants from this first set of calculations. From previous studies [25,26], it is known that a square lattice of circular holes can produce complete bandgaps with a hole filling fraction near $f = \pi/4 = 0.785$. Mechanical stability of the suspended membrane structure however, imposes practical limits on the filling fraction. For this reason, a filling fraction of 0.7 was selected for the structures in this study. In order to select the membrane thickness and PnC lattice constant, band structures as a function of the ratio of film thickness d to lattice constant a were calculated. As noted by others [25], it was found that the size of complete bandgaps is non-monotonic with respect to d/a, as seen in Figure 2.3c. Thus, a complete bandgap is absent in very thick and, perhaps counter-intuitively, also very thin membranes. From the plot in Figure 2.3c, we see that one maximum in bandgap width $\Delta\omega/\omega$ appears at around $d/a = 0.4 - 0.5$. The value $d/a = 0.5$ was chosen here. Additionally, the center of the desired bandgap was set to the frequency of dominant thermal phonons at 100 mK. Using the 2D Debye model, $\hbar\omega_{dom,2D} = 1.594 k_B T$, giving $\nu = \omega/(2\pi) \approx 3.2$ GHz.

In Figure 2.4a,b and c, we compare the dispersion relations of a full (un-perforated) SiN membrane of thickness $d = 485$ nm and two square lattice

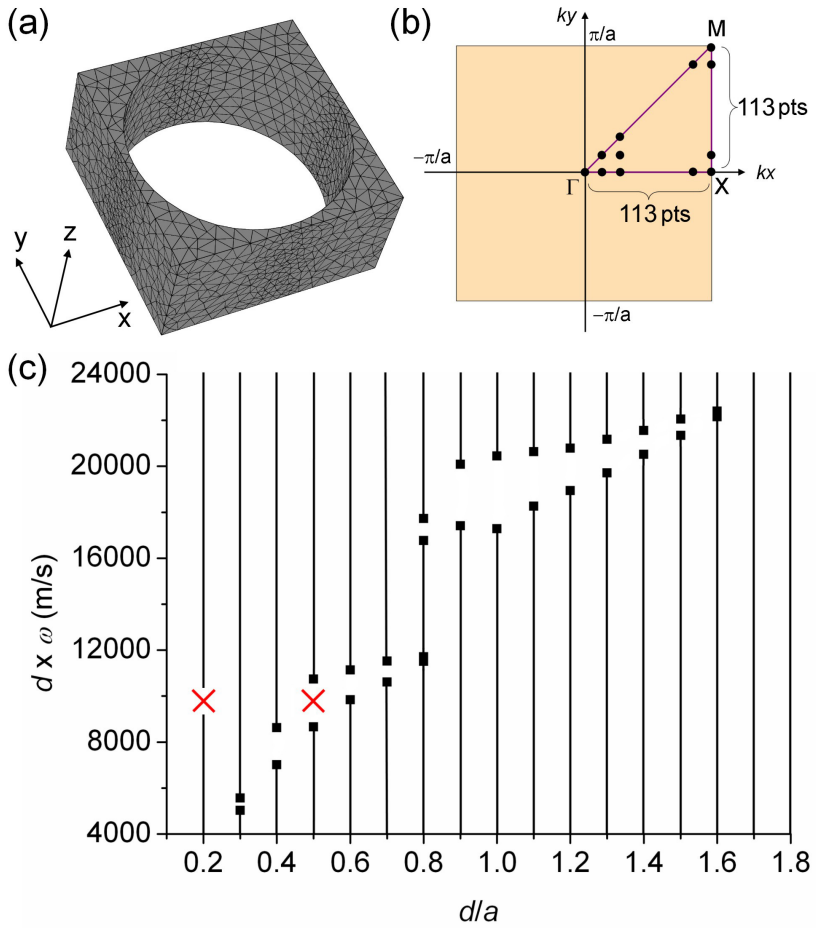

Figure 2.3: (a) A typical unit cell, with a filling factor $f = 0.7$, used in FEM calculations is shown. A typical mesh structure is also shown. (b) Wavevector k was varied within the first octant of the Brillouin zone (orange). Symmetry of the lattice allows the remaining octants to be filled using the data from the first. (c) Dependence of frequency spectrum on the ratio of membrane thickness d to lattice constant a is shown. The open regions indicate the size of the full band gap and red crosses mark the two design values selected for experiments.

PnCs on membranes of the same thickness. Dispersion relations are shown in the main symmetry directions Γ – X – M – Γ up to $\omega = 120$ rad/s (frequency $\nu = \omega/(2\pi) = 19$ GHz). Approximately 99% of the populated phonons at 0.1 K are contained in this range, thus Figure 2.4 gives a full picture of all the modes that affect thermal transport at that temperature. Obvious differences can be seen between the band structures. The PnC membrane with period 970 nm has the bandgap at $\nu = 3.3$ GHz as designed, and a width of 0.7 GHz. The bandgap width is only a small fraction of the range plotted, implying the gap itself has only a minor effect on thermal transport. Both PnCs however, display much flatter bands, which will affect the group velocities $\delta\omega/\delta k$ and the DOS.

The DOS for a full membrane and both PnC membranes are plotted in

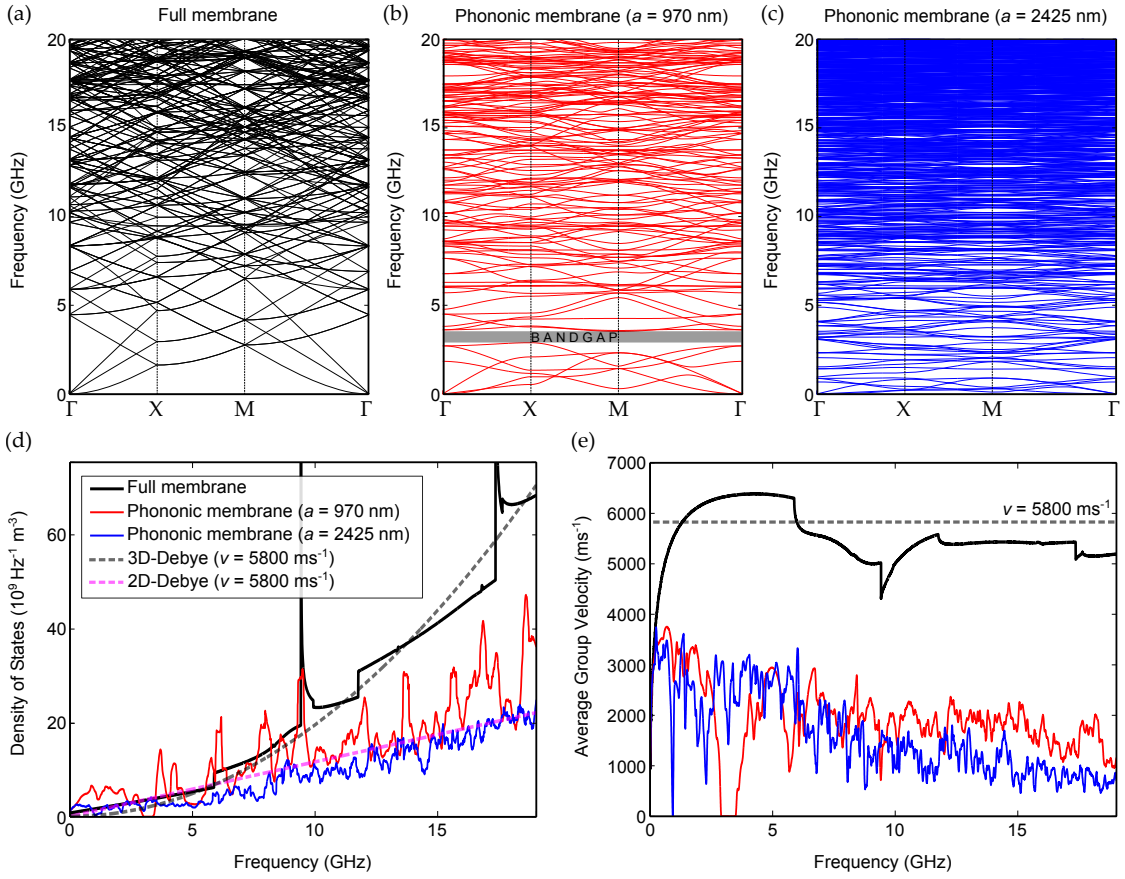

Figure 2.4: Dispersion relations are shown for the full membrane (a), PnC with a = 970 nm (b) and PnC with a = 2425 nm (c). DOS calculations (d) and average group velocity (e) for each of the three samples is shown.

Figure 2.4d using all k-values up to 19 GHz. It can be seen that the full membrane follows the 2D Debye model with DOS $\propto \omega$ up to $\nu \simeq 6$ GHz and begins to grow faster approximately $\propto \omega^2$ at higher frequencies, roughly in agreement with the 3D Debye model. This is an indicator of the 2D-3D transition for SiN membranes of thickness 485 nm, where higher order "optical" Lamb-modes begin to contribute. The DOS for both PnC membranes roughly follows the 2D Debye model up to 19 GHz without such a transition. Below the bandgap, the smaller period structure has a higher DOS than the full membrane. This will play an important role in heat conduction, as discussed below.

Group velocities for the three samples are plotted in Figure 2.4e. Average group velocities are lower in the PnC membranes and thus, with the DOS differences, a suppression of thermal conductance for both Pnc structures is expected at $T > 0.1$ K. This suppression is expected to grow with increasing temperature due to the lack of 2D-3D transition in the PnC membranes. At very low frequencies (temperatures), the group velocity and DOS effects are so small in

the PnCs that thermal conductance is expected to approach the full membrane result.

2.3.1 Measurement Scheme

Once samples were prepared and taken from the cleanroom, they were attached and bonded to the cryostat sample stage. Two bonding wires were used for each contact when possible. A bonded sample as viewed through the bonder microscope is shown in Figure 2.5a.

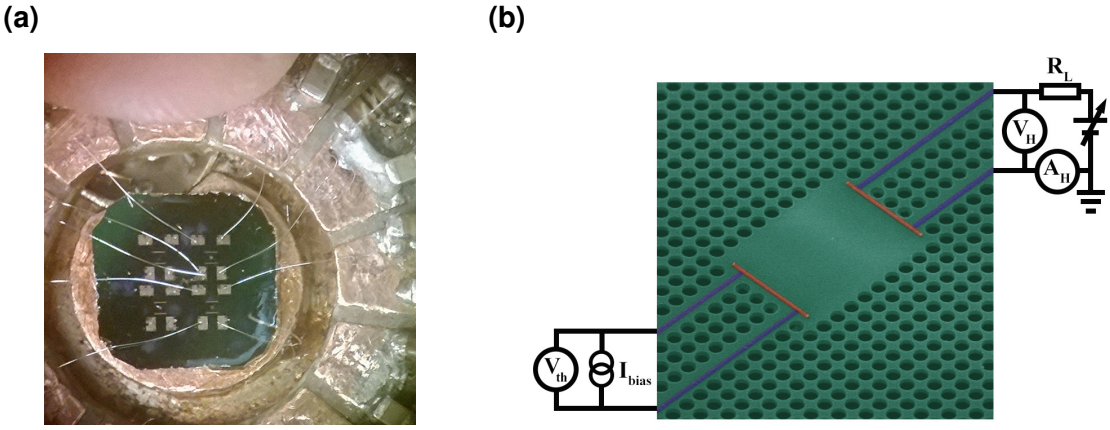

Figure 2.5: (a) Bonded sample chip is shown as seen through the bonder microscope. The chip is approximately 8 mm x 8 mm. (b) The measurement scheme is shown on a closeup of one PnC sample device.

In the experiment, the basic task is to measure the temperature of one SINIS junction (thermometer) in response to an applied voltage on the other device (heater). The power dissipated in the heater was determined by simultaneously measuring both the current and voltage. Current was measured via an Ithaco 1211 current preamplifier and voltage with an Ithaco 1201 high input impedance differential voltage preamplifier. Since all on-chip leads up to the Cu wire are superconducting Al, all the heat is dissipated at the junctions in the middle of the membrane and heat flow is two-dimensional.

The thermometer SINIS was operated at a fixed current bias, chosen according to the temperature range in question. The temperature dependent voltage response of a SINIS junction with constant current bias is well understood [11, 13], as was discussed in Section 1.3.2. Additionally, the thermometer junctions were current biased with a high resistance (1-10 GΩ) bias resistor in order to maintain the bias current even in the sub-gap region of the junction where R_T can be as high as 1–10 MΩ.

Figure 2.6 below shows the measured dissipated power as a function of the temperature of the thermometer for two PnC samples with periods 970 nm (red circles) and 2425 nm (blue circles) as well as the non-perforated membrane sample (black circles) up to about 1 K.

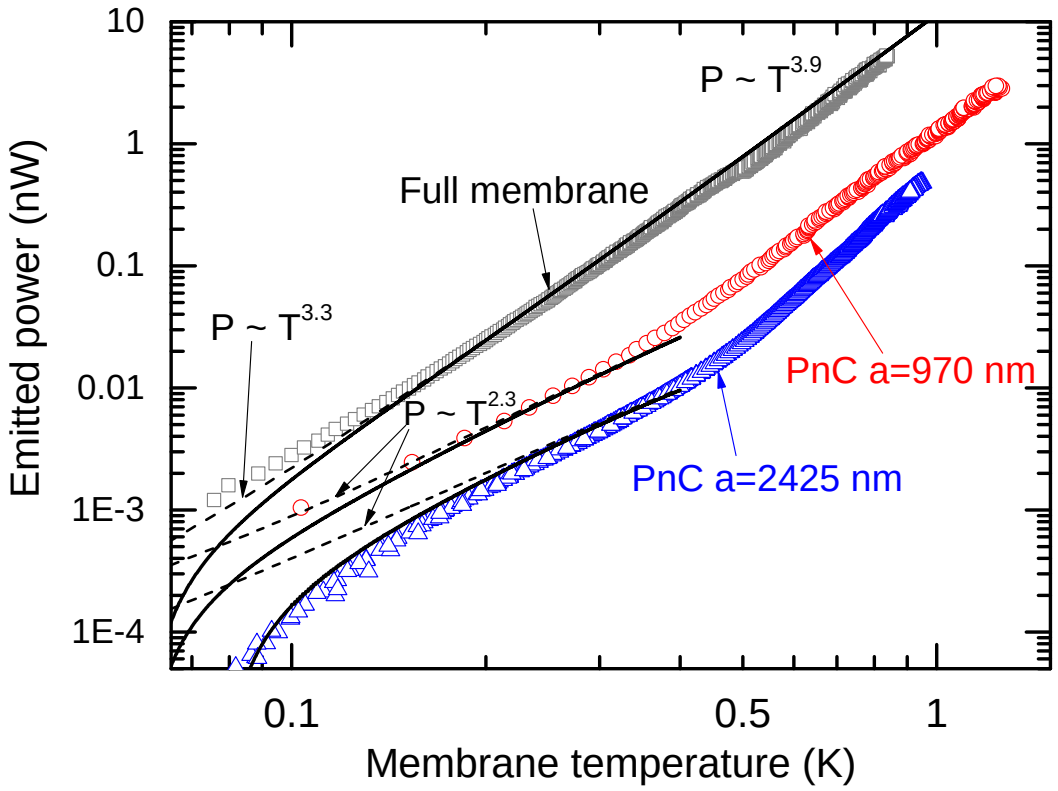

Figure 2.6: Measured dissipated power as a function of temperature of the thermometer for a full membrane sample (black circles), a PnC with period 970 nm (red circles) and a PnC with period 2425 nm (blue circles). A clear reduction of thermal conductance is seen in both PnC samples compared to the full membrane.

Dissipated power is clearly reduced for both PnC membranes compared to the full membrane at all temperatures. It is interesting to note that the larger lattice constant PnC shows a significantly lower emitted power though that geometry shows no bandgap, as seen in Figure 2.4c, indicating that bandgap size alone does not determine thermal conductance. Also, the conductance for the smaller period (larger period) PnC at low temperatures is about five (fourteen) times less than the full membrane, while at the high temperature end, the conductance is approximately eight (thirty) times less. In terms of thermal conductance defined as $G = P/\Delta T$, where $\Delta T = T_{meas} - T_{bath}$, we get conductances of $G \sim 6$ pW/K, ~ 30 pW/K and ~ 80 pW/K for the large period PnC, smaller period PnC and the full membrane respectively, at 0.1 K. These clear differences in temperature dependence of thermal conductance for the PnCs compared to the full membrane

rule out the possibility that diffusive scattering in bulk SiN is limiting thermal conductance [27].

Theoretical calculations for $P(T)$ are shown in Figure 2.6 as solid lines taking into account bath temperature phonon back radiation from the substrate and dashed lines without back radiation. Only one common scaling factor for P was used in fitting all three experimental curves. The agreement with measured temperature dependencies is very good all the way up to the highest temperatures calculated. For PnC membranes, computing resources limited this temperature to ~ 0.4 K. Since the heater dimensions were the same for all samples, the theory also predicts how much the power should be reduced in the PnC membrane compared to the full membrane. The data agree to a high degree with the predicted reduction giving strong evidence that the thermal conductance is dominated by the coherent band structure modifications rather than by scattering. With these results, we can clearly see that PnC devices offer a way to reduce thermal conduction significantly without having to reduce membrane thickness.

Chapter 3

3D Periodic Structures

3.1 Sample Fabrication for 3D Periodic Structures

3.1.1 Colloidal Self-Assembly

Of the many techniques for producing ordered arrays of nano-particles, our investigations centered around vertical deposition, or the so called Langmuir method. The process starts with silicon substrates either with or without a nitride (SiN_x) thin film. The SiN_x film can be used as an etch mask in further processing as described later. This substrate is then coated with a thin ($\sim$10 nm) layer of titanium in ultra-high vacuum, and exposed to $\sim$100 mbar oxygen pressure for 4 min to produce a titanium oxide TiO_x film. This serves as a hydrophilic surface for better wetting of the polystyrene (PS) nano-sphere solution.

Several variations of deposition parameters were investigated. Solutions of PS spheres having concentrations of 0.02%, 0.2%, 2%, 5% and 10% were used, with the lower concentrations being diluted from the original 10% solution purchased from Duke Scientific. Samples were vertically dipped into each solution and withdrawn at speeds from 0.01 mm/min up to 0.04 mm/min.

Patterned surfaces made by a two-step electron-beam lithography technique, shown schematically in Figure 3.1, were used to investigate lithographically assisted self-assembly. Samples were first coated on one side with two layers of 7% PMMA in anisole. Each layer was spin coated at 3500 rpm for 60 seconds and baked at 160 °C for 3 minutes. This resist was patterned with squares of sizes between 50 and 250 μm using e-beam exposure. The patterns were developed using MIBK for 50 seconds and rinsed in IPA for 30 seconds, then dried under nitrogen flow. Reactive ion etching (RIE) was used to etch the SiN through to the silicon underneath. Plasma parameters were 200 W and 30 mTorr with CHF_3 and O_2 flow rates at 50 and 5 sccm respectively. Using the SiN as an etch mask, square

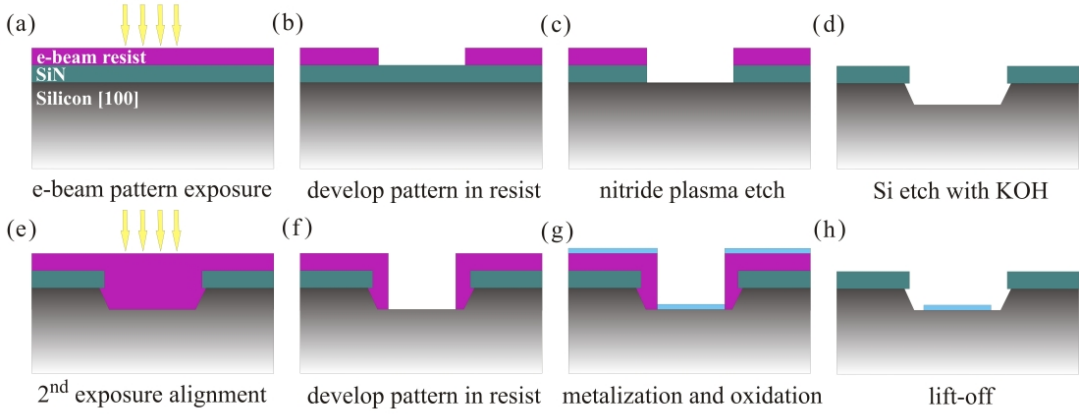

Figure 3.1: Lithography process steps are shown. (a) Pattern is exposed in e-beam resist (PMMA), (b) resist pattern is developed, (c) SiN_x is etched with CF_4 plasma and then (d) the Si substrate is etched anisotropically with KOH. (e) Second lithography is aligned with the previous pattern, (f) pattern is developed, (g) UHV evaporation of Ti and oxidation followed by (h) final lift-off.

pits were etched into the silicon with KOH. Etch temperature was kept at 90 °C for an etch rate of approximately 100 µm per hour (1.67 µm/min). Several samples were made with pits of depths from 5 µm to 30 µm. A layer of PMMA was spin coated on the etched side of the sample and square patterns were aligned with the bottom of etch pits. These patterns were developed in MIBK for 50 seconds, rinsed with IPA for 30 seconds and dried under nitrogen flow. A 10 nm layer of Ti was deposited by electron beam evaporation and oxidized in 100 mbar of oxygen pressure for 5 minutes. After lift-off, TiO_x was selectively left only at the bottom of the etch pits to serve as a hydrophilic surface. Finally, samples were coated with PS spheres using the technique desctibed in Section 1.4.5, filling the etch pits with multi-layer, self-assembled colloidal crystals.

3.1.2 Lithography on Colloidal Crystal Surface

Integrating measurement devices onto the colloidal crystal surface poses fabrication challenges. Many of the processes involved are known to partially damage or completely destroy PS spheres. Specifically, the baking of electron-beam resists occurs at temperatures above the normal glass transition of polystyrene, thus destroying the spherical shape. Additionally, the acetone used in standard lift-off of evaporated metals will very quickly dissolve polystyrene. One method for protecting the PS spheres from these damages is presented here.

It is known that UV and e-beam exposure causes cross-linking in polymers such as polystyrene [28]. We examined the use of electron-beam exposure to

modify the solubility and glass transition of polystyrene spheres. After depositing spheres on the substrate, samples were exposed by electron beam using 30 kV accelerating voltage. Most exposures were performed at 600 X magnification, resulting in exposed areas with dimensions 230 × 160 μm. The area dose was varied to find the optimal dose for hardening and exposed samples were immersed in acetone for several minutes. The exposed areas were protected from dissolution in the acetone while the surrounding areas were dissolved, as seen in Figure 3.2.

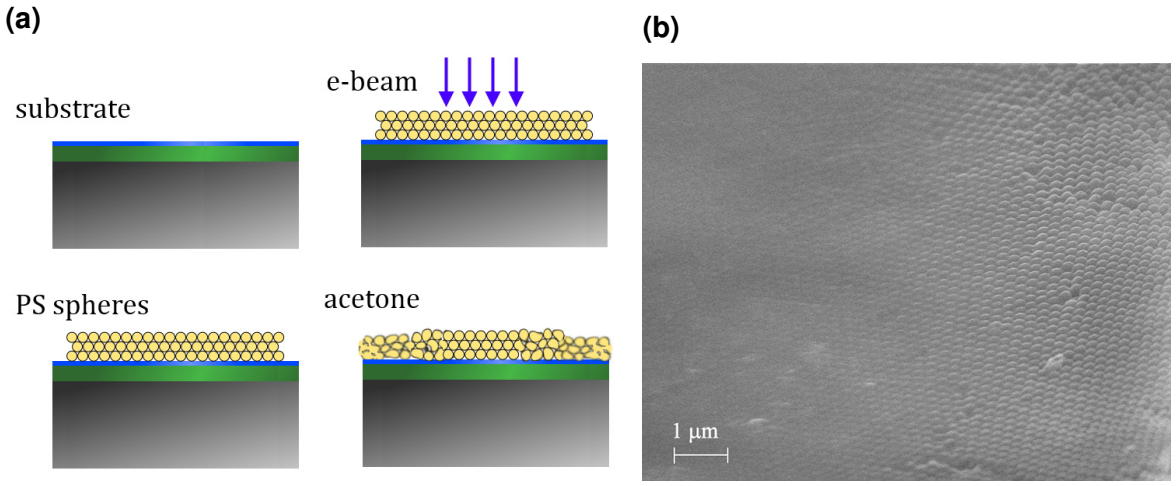

Figure 3.2: (a) Process steps for electron beam hardening of PS sphere colloidal crystals are shown. (b) The edge of an electron-beam exposure area shows a gradient of dissolution after immersion in acetone.

Deposition of electron beam evaporated metal wires was performed using samples given cross-linking area doses of ∼24 mC/cm^2 and immersed in acetone for 5 minutes. Electron beam evaporation was then used to coat the samples with a capping layer of AlO_x 50 – 100 nm thick. A layer of 9% PMMA in ethyl lactate followed by a layer of 4% PMMA in anisole were spin coated on the AlO_x capping layer. A simple wire pattern was exposed in the resist layers and developed in MIBK:IPA (1:3) for 50 seconds, then rinsed in IPA for 30 seconds and dried under nitrogen flow.

3.2 3D Theory

3.2.1 Colloidal Crystals

While photonic crystals have been a hot topic for decades in many areas of technological application, they can be found outside the laboratory in many

biological environments [29, 30]. The colorful inner coatings of various mollusk shells such as oyster, mussel and abalone are naturally formed by thin layers of aragonite (calcium carbonate) forming what is called nacre, or mother of pearl. The thickness of these optically translucent aragonite layers is in the range of visible light, which causes constructive and destructive interference for different wavelengths of light at different angles. This iridescence, or pearlescence, is not to be confused with opalescence, which is a "milky" appearance resulting from the refraction of light from ordered arrays of nano-scale spheres. Opals are naturally occurring photonic crystals composed of highly ordered spherical particles of silica (SiOx) ranging from highly ordered to nearly amorphous [31, 32]. There have been many developments in the fabrication techniques for self-assembly of micro and nano-crystals from colloidal suspensions. So while the general method has existed for millennia in nature, it has been known by scientists for just some decades.

3.2.2 Colloidal Self-Assembly

One of the most widely used nanoscale fabrication techniques is self-assembly. While the meaning of the term in general is straight forward, it can be used in many ways in different disciplines. Self-assembly in chemistry for example, describes the process of chemical bonding to form compounds and structures, usually in large and predictable numbers. In biology, the term is used in the context of spontaneous growth of molecular structures. In this work, the term refers to the un-aided ordering of pre-defined material components via physical means into large scale structures. To further specify the process used in this work, the term colloidal crystallization can be used. A colloidal suspension of particles is allowed to organize onto a substrate such that Brownian motion [33], capillary forces [17,34] and evaporation are the dominant factors influencing the final assembled structure.

3.3 3D Results

3.3.1 Finite Element Method Calculations

Starting from the Wigner-Seitz unit cell, we developed preliminary computer models of the self-assembled nano-sphere arrays using the finite element method (FEM) with a commercial code (COMSOL). Dispersion relations for the geometry were calculated using a Matlab script. We verified the results of the code against previous studies [35] done with the finite difference time domain (FDTD) method. Polystyrene density and speed of sound values were obtained from the Comsol material library.

The first Brillouin zone with symmetry points for the simple cubic (SC) lattice are shown in Figure 3.3a with the respective contacting sphere model geometry. Periodic boundary conditions satisfying Bloch's theorem are applied to the contact surfaces between neighboring spheres. The finite contact area aims to take into account the non-ideal contact between spheres in fabricated colloidal crystals as well as to avoid numerical problems with infinitesimal points.

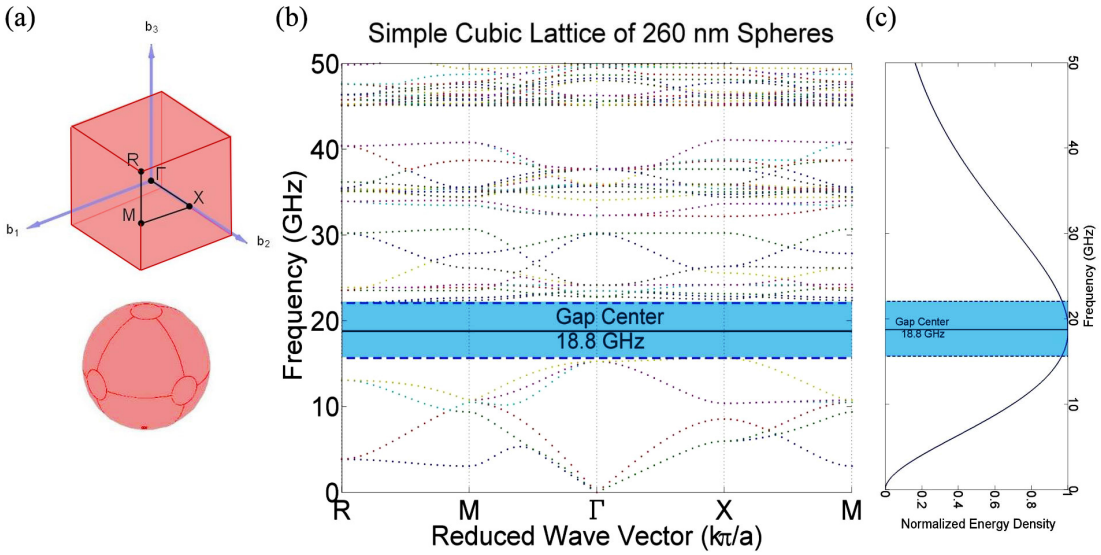

Figure 3.3: (a) The first Brillouin zone with symmetry points Γ, X, M, R. (b) The dispersion relation calculated for a simple cubic lattice of 260 nm diameter PS spheres shows a full bandgap of 6.4 GHz width centered at 18.8 GHz. (c) The center of this bandgap corresponds to the peak of the Debye energy density $g(\omega)$ at 50 mK.

A representative dispersion relation with a 6.4 GHz wide, full phononic bandgap centered at 18.8 GHz for the SC lattice with 260 nm diameter spheres is shown in Figure 3.3b. Also shown is the Debye spectral energy density, $g(\omega) = (3V\hbar/2\pi^2 v^3)\,[\omega^3(e^{(\hbar\omega/k_BT)} - 1)^{-1}]$ at 50 mK, in Figure 3.3c. It can be seen that for the SC lattice of spheres with diameter 260 nm, the central gap frequency corresponds to the peak in the Debye spectrum peak at 50 mK. This illustrates that by choosing the nano-sphere diameter correctly, it is possible to tailor the bandgap to coincide with the desired phonon energies.

During fabrication of the real colloidal crystals, soft spheres can undergo squeezing of varying degrees depending on the self-assembly conditions, while hard spheres are often sintered [33, 36] to fix them in place. The end result is spheres which contact each other not at an infinitesimal point, but through a finite contact area. To investigate the phononic band gap behavior of such non-ideal crystals in our model, we assumed a circular contact area between spheres. Then, the contact area between the spheres was varied by either increasing the size of the

sphere while maintaining the bounding unit cell or by maintaining the sphere size while reducing the bounding cell. Both methods gave qualitatively identical dispersion relations. The effect of contact area on the SC dispersion relation is shown in Figure 3.4.

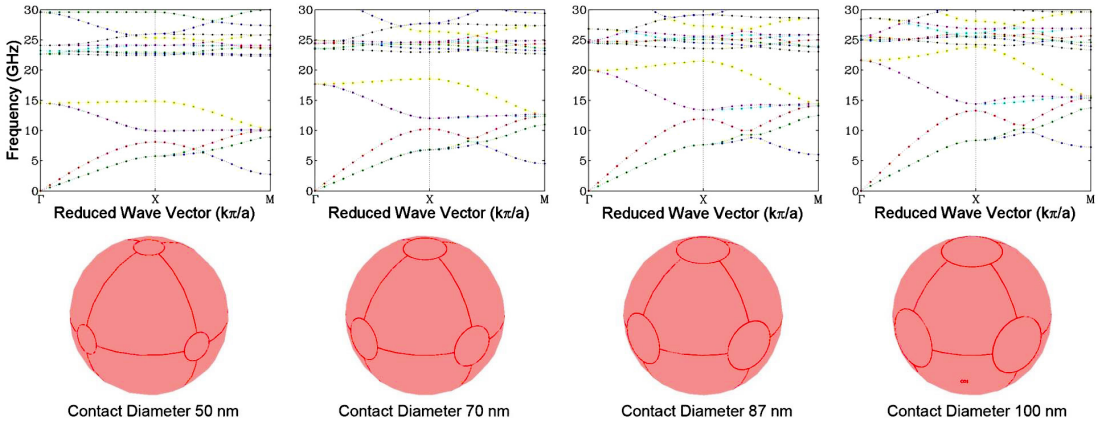

Figure 3.4: Comparison of dispersion relations in the Γ-X-M directions for varying contact area between spheres in a simple cubic lattice is shown. Contact diameters of 50, 70, 87 and 100 nm are presented. It can be seen that the band gap closes before the diameter of the contact area is half of the sphere diameter.

The calculations showed that an increased contact area resulted in a reduction of the band gap and an approach toward "bulk" behavior. Figure 3.4 shows a comparison of phononic band structures with varying contact area size for the SC lattice. We found that the gap closes rapidly; in fact, it is closed already at a contact diameter less than half of the sphere diameter. It seems that bulk-like dispersion behavior occurs long before the structure physically resembles a bulk.

3.3.2 Statistics of Colloidal Self-Assembly on Flat Surfaces

Typical colloidal crystal samples consisted of a set of domains, separated by cracks produced by the drying process. Domain size data were collected by taking several SEM images from each sample, and using the SEM scale bar as a calibration length, taking into account the dipping direction. Measurements taken along the dipping direction were defined as vertical lengths, while those which are perpendicular were defined as horizontal. A total of 2398 measurement pairs (horizontal and vertical lengths) were collected from over 50 SEM images to produce the statistical data. Representative SEM measurement images for three dipping speeds at three concentrations are shown in Figure 3.5. The image for each combination of dipping speed and concentration is marked with its respective average vertical domain length.

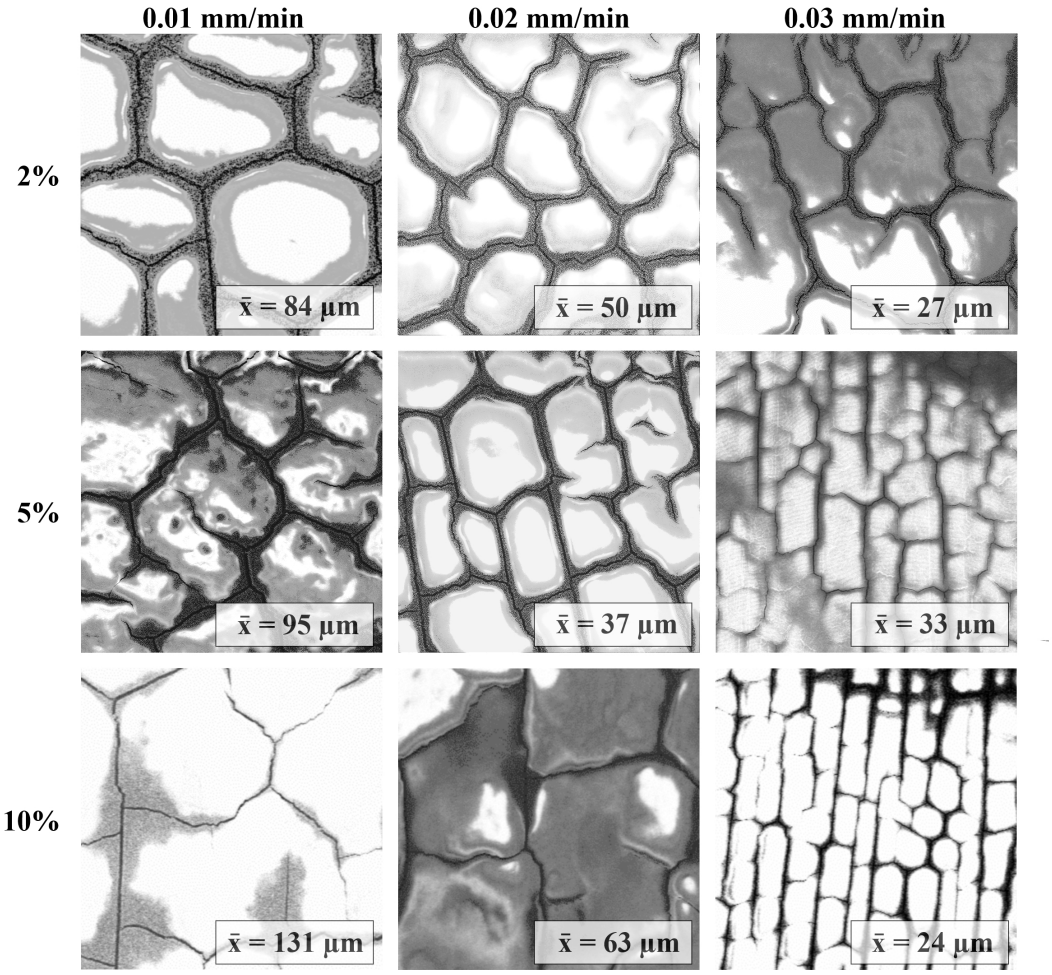

Figure 3.5: Representative measurement images are shown for different combinations of dipping speed and PS sphere concentrations. The average vertical domain length is noted for each combination. All images have the same scale.

Figure 3.6 shows a top view of a colloidal crystal structure (left) with its respective Fourier transformed k-space image (inset) showing well-ordered hexagonal symmetry. Also in Figure 3.6 (right), is a side-view close up of a thick multi-layer colloidal crystal displaying the typical face-centered 3D structure.

A clear trend toward larger average domains with increasing PS sphere solution concentration was accompanied by an increase in the size distribution. This large variability in domain size produced domains from a few tens of µm up to approximately 150 µm. Similar behavior was found for dipping speed, with domains ranging from several tens of µ up to approximately 350 µm.

Angled dipping was found to produce smaller domains on average. While the exact cause of this is unclear, it may be that changes in the shape of the meniscus can alter the evaporation rate at the self-assembly region. This could lead to shorter effective self-assembly times in the angled dipping cases.

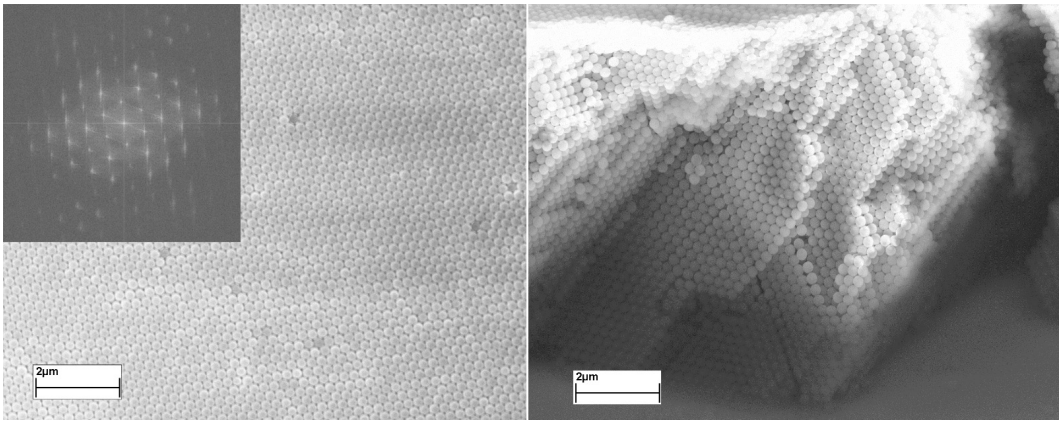

Figure 3.6: Top view of colloidal crystal structure with Fourier transformed image in the inset (left) with a side-view showing the 3D multi-layer colloidal crystal structure (right).

3.3.3 Log-Normal Domain Size Distributions

The domain size distributions for all dipping speeds and concentrations were analyzed, with example histograms of vertical domain lengths shown in Figure 3.7 for 2%, 5% and 10% concentrations at 0.01 mm/min dipping speed. We found all the concentrations were quite well characterized by log-normal size distributions (red curves), especially at the lowest dipping speeds. Only at the highest dipping speeds do the distributions start to be less skewed and approach the normal distribution.

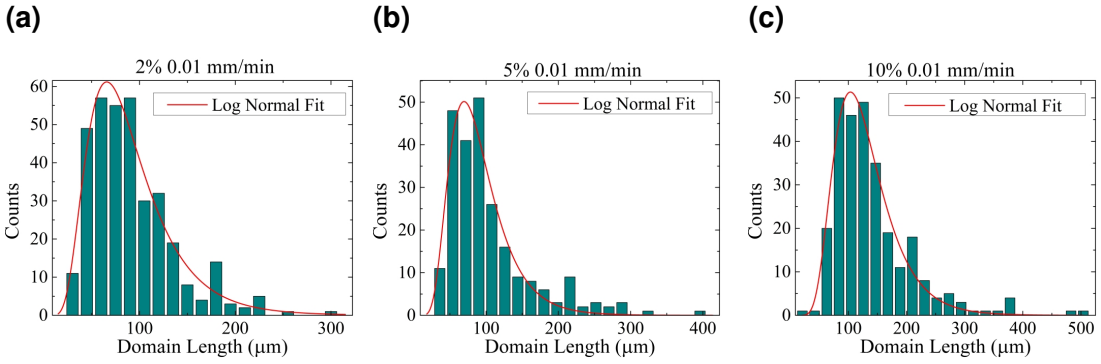

Figure 3.7: Histograms of vertical domain lengths are shown for (a) 2%, (b) 5% and (c) 10% concentrations at a dipping speed of 0.01 mm/min. All three concentrations are characterized by a log-normal size distribution.

Rather than the arithmetic mean and standard deviation, we calculated the geometric means $\bar{x}_g = (\Pi_n x_n)^{1/n}$ and the geometric standard deviations $\sigma_g = \exp\left(\sqrt{\sum_n (\ln^2(x_n/\bar{x}_g)/n)}\right)$ of these distributions and found that all σ_g values fell in the range of 1.32 and 1.71, with the exception of two anomalously wide

distributions. For 2% concentration and 0.02 mm/min dipping speed, the horizontal and vertical domain size distributions had deviations σ_g of 2.025 and 2.017, respectively. The normalized geometric standard deviations $\sigma_g/\bar{x}_g$ (Figure 3.8) are very well approximated by a $1/\bar{x}_g$ trend for all data points, except for the two anomalous $\sigma_g/\bar{x}_g$ values (circled in red) slightly farther from the fit curve. These two sets of data were likely the result of insufficient data sampling or poor substrate quality. The conclusion is, therefore, that the geometric standard deviation is constant for all dipping conditions.

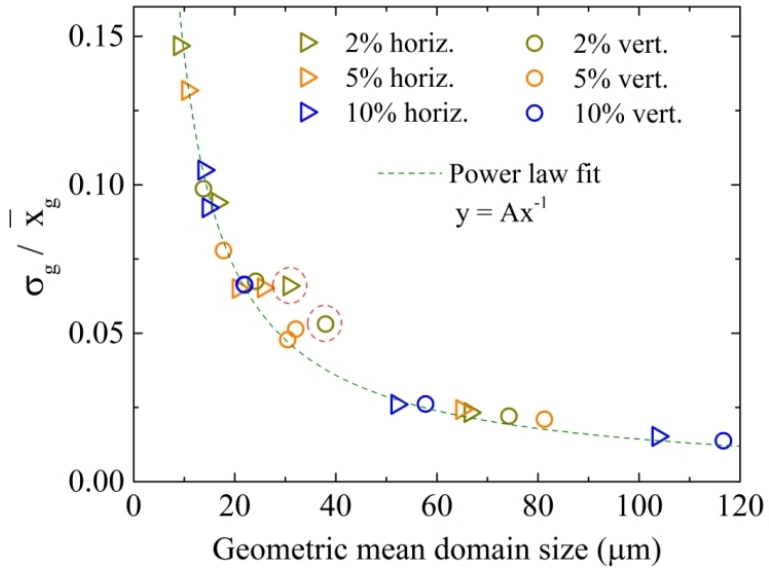

Figure 3.8: Normalized geometric standard deviation $\sigma_g/\bar{x}_g$ data for all dipping speeds and concentrations vs. geometric mean. Two anomalously wide distributions (circled in red) can be seen to fall farther from the $1/\bar{x}$ fit (dashed curve).

While log-normal size distributions are ubiquitous in biology, economics and material science [37], we are not aware of any previous reports on log-normal size distributions associated with colloidal crystal growth. Log-normality of grain sizes has been reported in atomic crystal growth of poly-crystalline thin films [38–40] and nanocomposites [41], and vapor phase growth of nanoparticles [42]. In addition, aggregation and fragmentation phenomena can also lead to log-normal distributions [43–48].

3.3.4 Deposition on lithographically pre-defined structures

The effects of etched lithographic features on self-assembly were studied by comparing domain size results of samples dipped at various speeds with troughs of varying size and depth. We patterned square troughs of side length varying

between 50 – 100 μm in steps of 10 μm and larger troughs from 150 to 300 μm in steps of 50 μm. Troughs of 10 μm depth showed hardly any change in domain sizes compared to areas outside the trough, while troughs of 30 μm depth did not appear to fill completely. All troughs of 20 μm depth consistently showed more order in general than unpatterned areas. Troughs smaller than 70 μm showed little to no difference in domain size when compared to the surrounding area while troughs larger than around 200 μm always contained more than one domain.

There are several studies on desiccation cracks in mud, clay and starch that relate crack spacing to layer thickness and crack pattern to desiccation process [46–48], with thicker layers forming cracks at greater spacing than thin layers. The drying of our colloidal crystal films may be similar to those drying processes, albeit on a much smaller scale, raising the question whether troughs are simply producing thicker layers and thus, larger domains. Indeed, for regions outside the troughs, the thickness of our colloidal crystals varies with dipping speeds (see Figure 3.9a), and thicker films do produce larger domains (see Figure 3.9b), but the nature of correlation between the film thickness and domain size is not linear for 10% concentration, as would be expected based on previous desiccation studies [46–48].

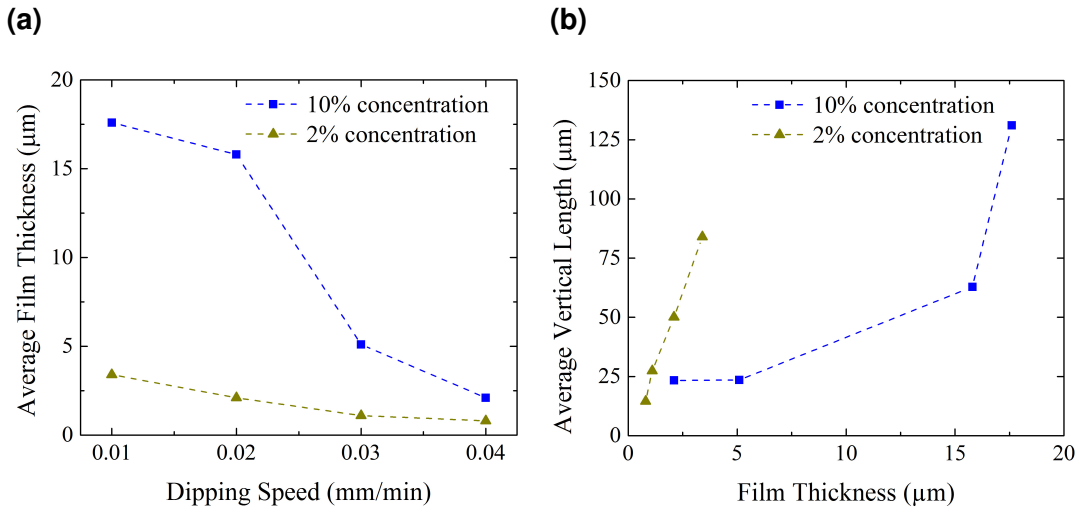

Figure 3.9: (a) Average film thickness is shown for 10% and 2% concentrations as a function of dipping speed. (b) Average vertical domain size is plotted against average film thickness for 10% and 2% concentrations.

Moreover, even though the thickness within the troughs is indeed higher than the surrounding areas, the lack of smaller domains inside the troughs points to a more direct effect, rather than just influence of the thickness. This also demonstrates that lithographically assisted self-assembly can be used to

consistently produce continuous regions of multi-layer colloidal crystal as large as 200 μm, effectively suppressing the size distributions found in unaltered substrates. While these regions are typically free of cracks, the crystalline quality of these lithographically assisted multi-layer structures is no better than that of the plain self-assembly samples. Improving the crystalline quality of these regions remains a significant challenge for rapid production of large-scale single-crystal structures.

3.3.5 Metal Deposition on Colloidal Crystal Surfaces

For lithographic testing purposes, a simple aluminum or copper film was deposited by electron beam evaporation on patterns of varying line width and lift-off performed. The resulting metal wires were then tested for electrical contact and inspected by SEM as seen in Figure 3.10.

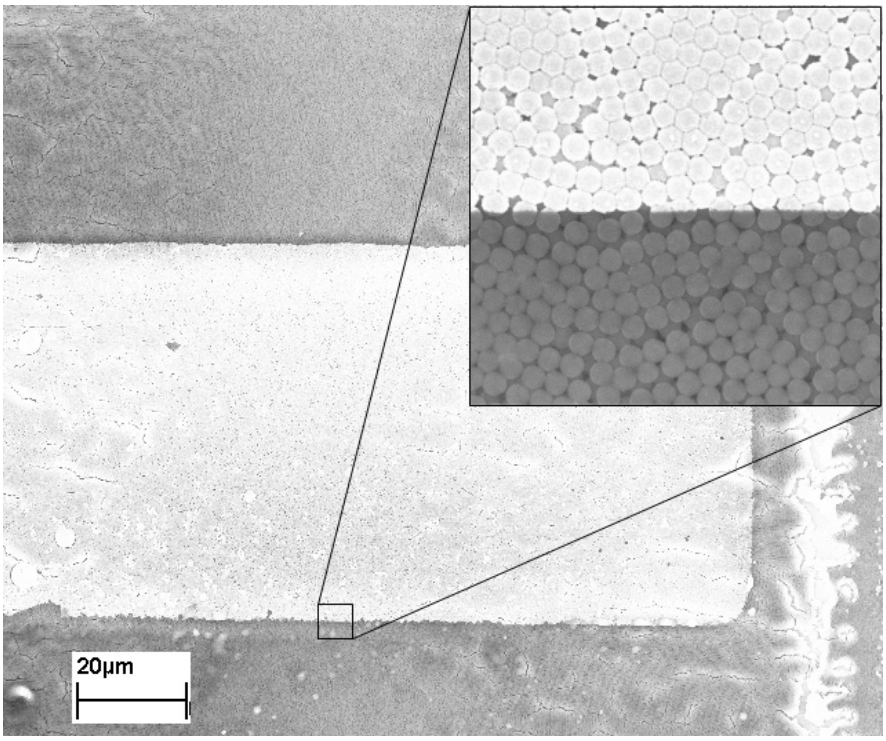

Figure 3.10: Aluminum wire deposited by electron beam evaporation is shown on top of a hardened PS sphere colloidal crystal with AlO_x capping layer. The roughness of the metal wire edge (inset) is seen to be less than the sphere size.

Roughness at the edge of wires, as seen in the inset in Figure 3.10, was found to be low enough to suggest the possibility of producing wires approaching the diameter of PS spheres. We have observed preliminary results of micrometer scale Al wires which are continuous and exhibit electrical conductivity. While sub-micron

wires have also been fabricated, there are still issues with wire continuity and thus, electrical conductivity. Further development in lithographic processing is expected to enable the fabrication of $\sim$500 nm wide conducting metal wires on the colloidal crystal surfaces.

Chapter 4

Suspended Beam Structures

This chapter details the preliminary investigation of boundary engineering for the improvement of bolometric detectors and tunnel junction coolers. Comparing the results of suspended and bulk tunnel junction devices as well as devices of different beam length, it was determined that ballistic phonon transport is the dominant heat flow mechanism at low temperatures in suspended nanostructures [11]. With this, it should be possible to control the cooling and heating properties of such junctions and devices through boundary engineering i.e., changing the shape of the contact between the suspended beam and the bulk. Additionally, we address fabrication issues related to the structural release of tunnel junction coolers and present a solution.

Suspended nanostructures are becoming increasingly important in modern integrated circuits. Nanoscale beams and membranes for example, can be found in a wide variety of ultra-sensitive low-temperature devices such as bolometers and calorimeters. Reducing the size of active components and material selection are often the methods used to increase the sensitivity and performance of these devices. Here, we suggest boundary engineering as a possible alternative or additional method to enhance performance.

4.1 Suspended Beam Sample Fabrication

Sample fabrication begins with 30-nm-thick silicon nitride (SiN) membranes fabricated by the bulk micromachining techniques described in Section 1.4.2. Tunnel junctions were fabricated on top of the membranes using EBL and UHV metal evaporation, as described in Section 1.4.3. After producing junctions, the membrane was etched through by RIE in CHF_3 plasma. The metal wires can serve as etch masks and often no additional lithography is needed for the structural

release of suspended nanowires. This results in the extent of the suspended structure being defined by the size of the membrane as seen in Figure 4.1 [11].

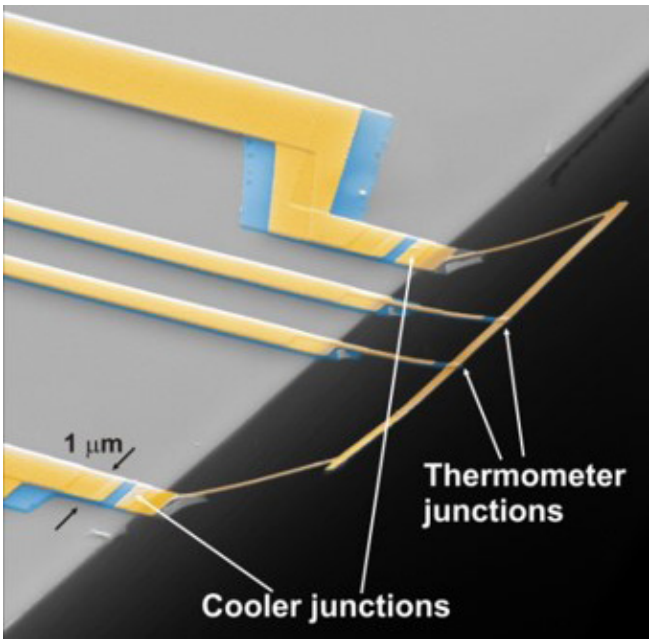

Figure 4.1: Scanning electron micrograph of a suspended nanowire sample. Yellow indicates Cu or Au (normal metal) and blue indicates Al (superconductor). Cooler junctions are located at the edge of the substrate, while thermometer junctions are at the center of the nanowire [11].

Aluminum wires were approximately 60 nm thick and 200 nm wide at their narrowest. The cooler junctions were approximately 0.35 μm^2 and were located on the bulk to avoid significant backflow of dissipated heat into the suspended normal metal wire. Thermometer junctions were approximately 0.05 μm^2 and were located on the suspended wire. As the phononic thermal conductance from suspended nanowire to bulk was found to be an order of magnitude smaller than the conductance between electrons and phonons, the thermal bottleneck in these samples was the phonon transmission. Therefore, the electrons and phonons are in quasiequilibrium and thus, thermometry and, more importantly, cooling apply to their common temperature. More details of the simplest 1D beam fabrication can be found in [11] and [49].

For more complicated boundary geometries, the nitride was etched in a lithographically defined area around the junctions. A protective layer of PMMA resist was spin coated on the samples and the etch area was patterned by EBL. Etch parameters for the lithographically patterned samples were the same as without patterning. Metal wires within the exposed area again served as etch masks to produce suspended nanowires of SiN and metal as seen in Figure 4.2. Such narrow

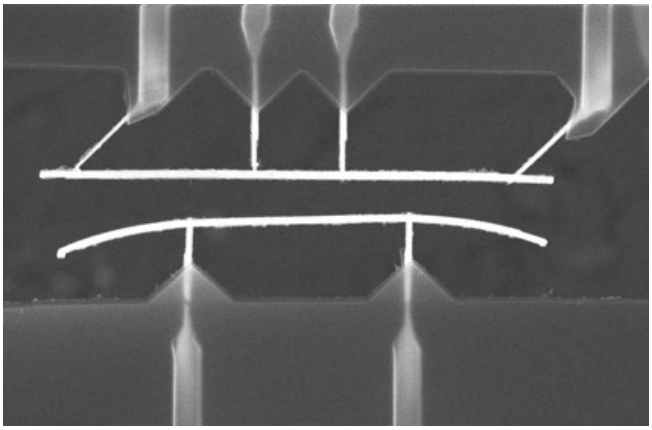

Figure 4.2: SEM image of a boundary engineered sample with suspended metal nanowires and tapered SiN supports at the boundary between nanowire and membrane.

beams cannot survive the mechanical stresses of typical lift-off procedures and thus, require a more gentle method for removing the PMMA residue after etching. Critical point drying (CPD) with CO_2 was used to remove the samples from the lift-off fluids without exposing the beams to the surface tension forces. While this dramatically improved yield, an unexpected issue with the Cu wires arose.

It was discovered, that junctions made using Cu as the normal metal were degraded by the post-etch processing steps, often resulting in junction resistances in excess of 10 MΩ. There was some evidence that the high pressure of the critical point drying process contributed to the degradation, as shown in Figure 4.3.

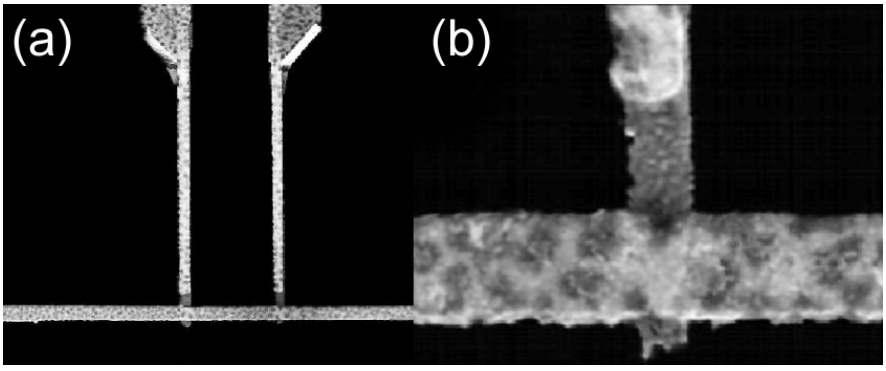

Figure 4.3: SEM image of a sample with Cu after CPD lift-off. Degradation of film quality arising from high pressure is visible in the closer view (b). The high resistances of post-CPD nanowires make them unsuitable for measurements.

However, it is also known that solvents, such as acetone and those found in PMMA resists, can have damaging effects on Cu films [50]. In addition to the effects of acetone, we found that Cu was partially or even completely removed after resist baking, indicating that the metal is susceptible to degradation in heated

solvents such as chlorobenzene, anisole and ethyl lactate. This issue was addressed in suspended nanowire samples by replacing the Cu with gold (Au). Similar difficulties with Cu films were experienced in 2D samples, which are detailed in Chapter 2.

4.2 Theory for Suspended Beams

4.2.1 Thermal Transport in Nanoscale Beams

Suspended beams, such as those pictured in Figures 4.1 and 4.2, can be considered one-dimensional (1D) if they have width and thickness less than the wavelength of dominant thermal phonons

$$\lambda_T = \frac{hc}{2.82k_BT}\,, \tag{4.1}$$

where h, c, k_B and T are Planck's constant, the average velocity of sound in the material, the Boltzmann constant and temperature respectively. In the low temperature limit, only the four lowest modes are occupied. In other words, while the higher modes do not contribute to thermal transport, each of these four lowest modes always contribute the quantum of thermal conductance G_0 given by

$$G_0 = \frac{\pi^2 k_B^2}{3h}T\,, \tag{4.2}$$

if perfect transmission from the beam to the substrate is assumed. In 2000, Schwab et al. demonstrated experimentally that, by shaping a nanoscale beam as a catenoid, one could produce an ideal ballistic phonon conductor with unity transmission [51]. Suspending a thin SiN membrane by four catenoid beams allowed them to measure a thermal conductance of $16G_0$, with four beams each supporting four modes [51].

This description becomes complicated by the existence of a non-catenoidal contact from suspended beam to membrane or to bulk. Strong scattering at an abrupt contact will lower the conductance from the quantum value and the power law for the temperature dependence of the conductance will be changed. In the case of the structures in question here, the beams contact the membrane or the bulk at 90° with sharp corners and thus, there is a change in phonon dimensionality at the interface. The temperature dependence of thermal conductance G_{Th} through a 1D contact to either a 2D or 3D reservoir is given by [52, 53]

$$G_{Th}^{1D-2D} \propto T^{1.5-2.5} \qquad \text{or} \qquad G_{Th}^{1D-3D} \propto T^{3-5}\,, \tag{4.3}$$

where the exponent depends on which phonon mode is dominant.

4.3 Suspended Beam Results

4.3.1 Tunnel Junction Cooling

The cooling of both electrons and phonons in suspended beams was reported by Koppinen and Maasilta in [11]. Suspended structures displayed significantly greater cooling compared to bulk cooler results. The reduced dimensions of the suspended nanowire ensured that phonon transport was the bottleneck in thermal conductance. Figure 4.4 shows measurement results of cooling experiments for various device geometries.

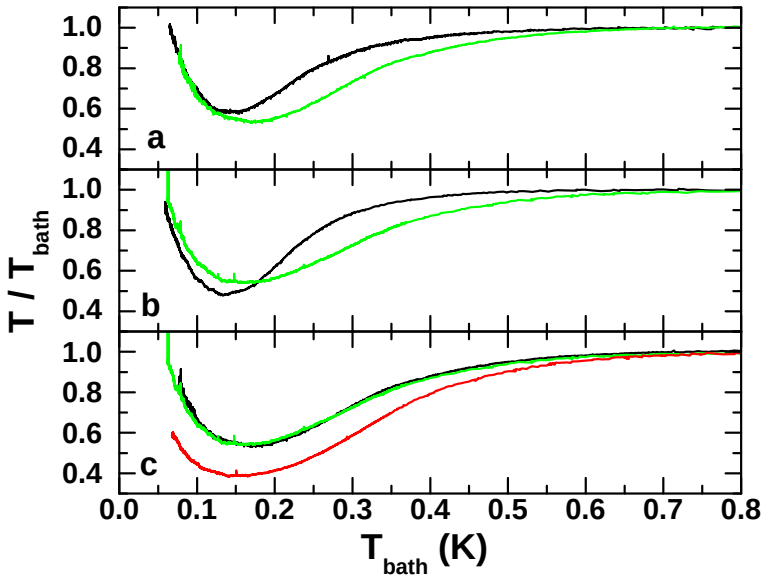

Figure 4.4: (a) Temperature of cooled suspended (green) and bulk (black) 20 μm long nanowires normalized with the bath temperature T/T_{bath} vs T_{bath}. The cooler is biased to the optimal cooling voltage, while the bath temperature is changed. Both samples have an electron gas volume $\Omega = 0.17$ μm^3 and tunneling resistance is R_T ∼3 kΩ for the suspended and R_T ∼4.4 kΩ for the bulk sample. At the low-temperature regime, cooling efficiency is limited by the junctions, whereas at higher temperatures cooling behavior is different due to the different dissipation mechanisms (e-ph interaction for bulk samples vs. phonon transport for suspended samples). (b) The same as (a), but for longer 30-μm-long wires with $\Omega = 0.36$ μm^3 and R_T ∼3 kΩ. (c) The same, comparing the two suspended samples in (a) (black) and (b) (green) with a third suspended sample (red) with $\Omega = 0.36$ μm^3 and R_T ∼1.7 kΩ. [11]

In Figure 4.4a, a comparison between a 20 μm long suspended (green) and bulk (black) nanowire demonstrates that suspended samples allow greater cooling. The longer (30 μm) suspended and bulk nanowire data in Figure 4.4b again confirm that

suspended samples have greater cooling. Figure 4.4c compares the two suspended coolers from (a)(black) and (b)(green) with a third suspended sample (red) having volume $\Omega = 0.36$ μm^3 and $R_T \sim 1.7$ kΩ. It is clear that the normal metal volume does not affect the cooling, while the tunneling resistance does. The size independence verifies that there are no 1D [54] or 3D [55] electron-phonon interaction limits to heat flow. In addition, no thermal gradient was observed between the center of the wire and the end. Thus, it seems likely that it is phonon transmission at the interface between nanowire and bulk which limits heat flow.

The fabrication of the cooler junctions on the bulk as opposed to on the suspended nanowire reduced the backflow of dissipated heat and thus increased the cooling power [56]. Cooling was demonstrated for both Cu and Au normal metal wires [57]. Cooling from 115 mK to 70 mK with Au normal metal wire is presented in Figure 4.5. From these results, we verified that the processing difficulties do not rule out boundary engineering with tunnel junction coolers.

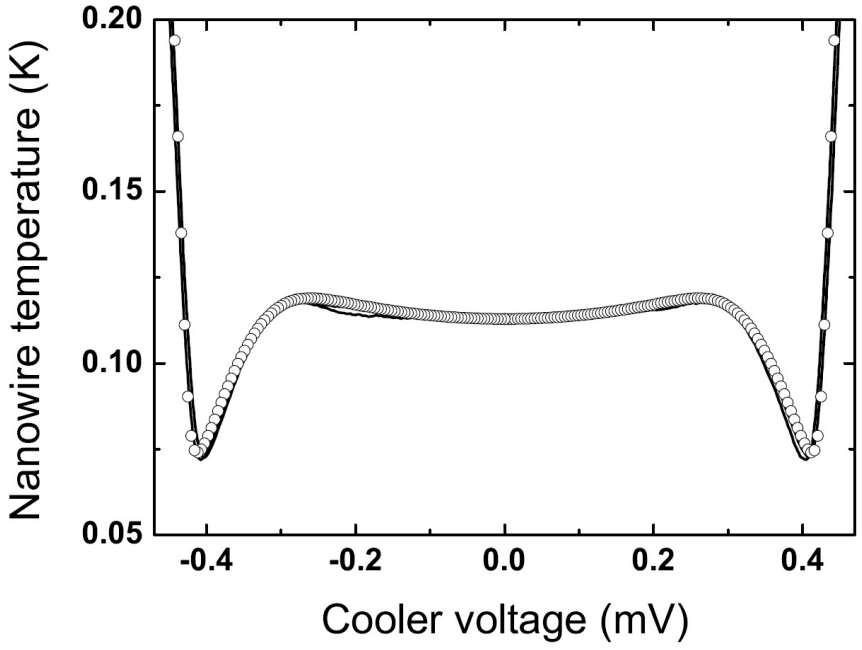

Figure 4.5: Cooling from 115 mK to 70 mK on a suspended beam with Au as the normal metal is shown. [57]

A complementary heating experiment without cooler tunnel junctions but with the same nanowire width w = 300 nm and thickness t = 60 nm (length was L = 24 μm) further verified the thermal transport behavior. In that experiment, the cooler tunnel junctions were substituted by direct contact between the normal metal (Cu) and a superconductor (Nb). These NS junctions work as good electrical contacts but also as nearly perfect thermal barriers meaning that Joule heating

power $P_{in} = IV$ is dissipated uniformly in the normal metal and $P_{in} = A(T_{nw}^n - T_{bath}^n)$. Figure 4.6 shows the result of a heating experiment, where the temperature of the nanowire is plotted as a function of the heating power in log-log scale. We notice that the data are well described by a transition from a power law with n = 2.8 at low temperatures to a power law with $n \approx 6$ at high temperatures. The low-temperature exponent n = 2.8 is consistent with the theory of 1D–2D interface scattering [52].

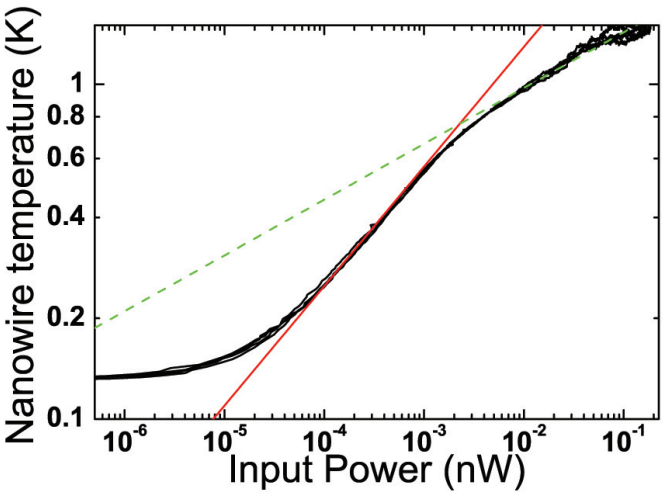

Figure 4.6: Heating experiment: temperature of a suspended nanowire as a function of input dc power. Red and green dashed lines correspond to power laws $n = 2.8$ and $n = 6$, respectively. The low-temperature saturation is likely due to absorbed noise power of ∼6 fW. A = 4.3 pW/K$^{2.8}$ for the low-temperature power law $n = 2.8$.

Bibliography

[1] BAILEY, C. (ed.), *Advanced Cryogenics*, The International Cryogenics Monograph Series (Plenum Press, London, 1971).

[2] KITTEL, C., *Introduction to Solid State Physics* (John Wiley and Sons, New York, 1996), 7th ed.

[3] CLELAND, A., *Foundations of Nanomechanics* (Springer, Berlin, 2003).

[4] POBELL, F., *Matter and methods at low temperatures* (Springer, Berlin, 1996), 2nd ed.

[5] ULLOM, J., *Physics and applications of NIS junctions*. AIP Conference Proceedings **605** (2001) 135–140.

[6] TINKHAM, M., *Introduction to Superconductivity*, International Series in Pure and Applied Physics (McGraw-Hill, New York, 1975).

[7] KIVIOJA, J., *Mesoscopic Superconducting Tunnel Junction Devices*, Ph.D. thesis, Helsinki University of Technology, Espoo, Finland (2005).

[8] KOPPINEN, P. J., KÜHN, T., AND MAASILTA, I. J., *Effects of charging energy on sinis tunnel junction thermometry*. Journal of Low Temperature Physics **154** (2009) 179–189.

[9] PEKOLA, J. P., MAISI, V. F., KAFANOV, S., CHEKUROV, N., KEMPPINEN, A., PASHKIN, Y. A., SAIRA, O.-P., MÖTTÖNEN, M., AND TSAI, J. S., *Environment-assisted tunneling as an origin of the dynes density of states*. Physical Review Letters **105** (2010) 026803.

[10] KARVONEN, J., TASKINEN, L., AND MAASILTA, I., *Influence of temperature gradients on tunnel junction thermometry below 1 k: Cooling and electron-phonon coupling*. Journal of Low Temperature Physics **146** (2007) 213–226.

[11] KOPPINEN, P. AND MAASILTA, I., *Phonon cooling of nanomechanical beams with tunnel junctions*. Physical Review Letters **102** (2009) 165502.

[12] MESCHKE, M., GUICHARD, W., AND PEKOLA, J., *Single-mode heat conduction by photons*. Nature **444** (2006) 187–190.

[13] GIAZOTTO, F., HEIKKILÄ, T., LUUKANEN, A., SAVIN, A., AND PEKOLA, J., *Opportunities for mesoscopics in thermometry and refrigeration: Physics and applications*. Reviews of Modern Physics **78** (2006) 217–274.

[14] TASKINEN, L., KIVIOJA, J., KARVONEN, J., AND MAASILTA, I., *Direct measurement of the electron-phonon relaxation rate in thin copper films*. Physica Status Solidi C **1** (2004) 2856–2859.

[15] KARUPPUCHAMY, S. AND JEONG, J. M., *Super-hydrophilic amorphous titanium dioxide thin film deposited by cathodic electrodeposition*. Materials Chemistry and Physics **93** (2005) 251–254.

[16] JIANG, P., BERTONE, J. F., HWANG, K. S., AND COLVIN, V. L., *Single-crystal colloidal multilayers of controlled thickness*. Chemistry of Materials **11** (1999) 2132–2140.

[17] DENKOV, N., VELEV, O., KRALCHEVSKI, P., IVANOV, I., YOSHIMURA, H., AND NAGAYAMA, K., *Mechanism of formation of two-dimensional crystals from latex particles on substrates*. Langmuir **8** (1992) 3183–3190.

[18] DENKOV, N., VELEV, O. D., KRALCHEVSKY, P. A., IVANOV, I. B., YOSHIMURA, H., AND NAGAYAMA, K., *Two-dimensional crystallization*. Nature **361** (1993) 26–26.

[19] ZHANG, J., SUN, Z., AND YANG, B., *Self-assembly of photonic crystals from polymer colloids*. Current Opinion in Colloid & Interface Science **14** (2009) 103–114.

[20] LI, Z., WANG, J., AND SONG, Y., *Self-assembly of latex particles for colloidal crystals*. Particuology **9** (2011) 559–565.

[21] IRWIN, K. D., HILTON, G. C., WOLLMAN, D. A., AND MARTINIS, J. M., *X-ray detection using a superconducting transition-edge sensor microcalorimeter with electrothermal feedback*. Applied Physics Letters **69** (1996) 1945–1947.

[22] KARVONEN, J., KÜHN, T., AND MAASILTA, I., *Temperature profile for ballistic and diffusive phonon transport in a suspended membrane with a radially symmetric heat source*. Chinese Journal of Physics **49** (2011) 435–442.

[23] HOEVERS, H. F. C., RIDDER, M. L., GERMEAU, A., BRUIJN, M. P., DE KORTE, P. A. J., AND WIEGERINK, R. J., *Radiative ballistic phonon transport in silicon-nitride membranes at low temperatures*. Applied Physics Letters **86** (2005) 251903.

[24] HOLMES, W., GILDEMEISTER, J. M., RICHARDS, P. L., AND KOTSUBO, V., *Measurements of thermal transport in low stress silicon nitride films*. Applied Physics Letters **72** (1998) 2250.

[25] PENNEC, Y., VASSEUR, J., DJAFARI-ROUHANI, B., DOBRZYNSKI, L., AND DEYMIER, P., *Two-dimensional phononic crystals: Examples and applications*. Surface Science Reports **65** (2010) 229–291.

[26] MALDOVAN, M. AND THOMAS, E., *Simultaneous complete elastic and electromagnetic band gaps in periodic structures*. Applied Physics B **83** (2006) 595–600.

[27] RAYLEIGH, L., *On the influence of obstacles arranged in rectangular order upon the properties of a medium*. Philosophical Magazine **34** (1892) 481–502.

[28] SCHNABEL, W. AND SOTOBAYASHI, H., *Polymers in electron beam and x-ray lithography*. Progress in Polymer Science **9** (1983) 297–365.

[29] VUKUSIC, P., SAMBLES, J., AND LAWRENCE, C. R., *Structural colour: Colour mixing in wing scales of a butterfly*. Nature **404** (2000) 457.

[30] VUKUSIC, P. AND SAMBLES, J. R., *Photonic structures in biology*. Nature **424** (2003) 852.

[31] COLE, S. H. AND MONROE, E. A., *Electron microscope studies of the structure of opal*. Journal of Applied Physics **38** (1967) 1872–1873.

[32] JONES, J. B., SANDERS, J. V., AND SEGNIT, E. R., *Structure of opal*. Nature **204** (1964) 990.

[33] XIA, H. AND WANG, D., *Fabrication of macroscopic freestanding films of metallic nanoparticle monolayers by interfacial self-assembly*. Advanced Materials **20** (2008) 4253–4256.

[34] FUSTIN, C. A., GLASSER, G., SPIESS, H. W., AND JONAS, U., *Parameters influencing the templated growth of colloidal crystals on chemically patterned substrates*. Langmuir **20** (2004) 9114–9123.

[35] HSIEH, P.-F., WU, T.-T., AND SUN, J.-H., *Three-dimensional phononic band gap calculations using the fdtd method and a pc cluster system*. Ultrasonics, Ferroelectrics and Frequency Control, IEEE Transactions on **53** (2006) 148–158.

[36] MÍGUEZ, H., MESEGUER, F., LÓPEZ, C., BLANCO, íA., MOYA, J. S., REQUENA, J., MIFSUD, A., AND FORNÉS, V., *Control of the photonic crystal properties of fcc-packed submicrometer sio2 spheres by sintering*. Advanced Materials **10** (1998) 480–483.

[37] AITCHESON, J. AND BROWN, J. A. C. (eds.), *The lognormal distribution* (Cambridge University Press, Cambridge, 1969).

[38] KURTZ, S. K. AND CARPAY, F. M. A., *Microstructure and normal grain growth in metals and ceramics. part II experiment*. Journal of Applied Physics **51** (1980) 5745–5754.

[39] ESPIAU DE LAMAESTRE, R. AND BERNAS, H., *Significance of lognormal nanocrystal size distributions*. Physics Review B **73** (2006) 125317.

[40] BERGMANN, R. B. AND BILL, B., *On the origin of logarithmic-normal distributions: An analytical derivation, and its application to nucleation and growth processes*. Journal of Crystal Growth **310** (2008) 3135–3138.

[41] LU, C., Y.-H. LU, Y.-H., SHEN, Y.-G., AND MAI, Y.-W., *Log-normal nanograin-size distributions in nanostructured composites*. Philosophical Magazine Letters **88** (2008) 829–836.

[42] SÖDERLUND, J., KISS, L. B., NIKLASSON, G. A., AND GRANQVIST, C. G., *Lognormal size distributions in particle growth processes without coagulation*. Physical Review Letters **80** (1998) 2386–2388.

[43] EPSTEIN, B., *The mathematical description of certain breakage mechanisms leading to the logarithmco-normal distribution*. Journal of the Franklin Institute **244** (1947) 471–477.

[44] LEE, K. W., LEE, Y. J., AND HAN, D. S., *The log-normal size distribution theory for brownian coagulation in the low knudsen number regime*. Journal of Colloid and Interface Science **188** (1997) 486–492.

[45] GMACHOWSKI, L., *Aggregate structure and size distribution at steady state shear aggregation*. Colloids and Surfaces A **201** (2002) 41–46.

[46] GROISMAN, A. AND KAPLAN, E., *An experimental study of cracking induced by desiccation*. Europhysics Letters **25** (1994) 415–420.

[47] COLINA, H. AND ROUX, S., *Experimental model of cracking induced by drying shrinkage*. European Physical Journal E **1** (2000) 189–194.

[48] BOHN, S., PLATKIEWICZ, J., ANDREOTTI, B., ADDA-BEDIA, M., AND COUDER, Y., *Hierarchical crack pattern as formed by successive domain divisions. II. From disordered to deterministic behavior*. Phys. Rev. E **71** (2005) 046215.

[49] KOPPINEN, P. J., *Applications of Tunnel Junctions in Low-Dimensional Nanostructures*, Ph.D. thesis, University of Jyväskylä (2009).

[50] KAGWADE, S., CLAYTON, C., CHIDAMBARAM, D., AND HALADA, G., *Photochemical breakdown of acetone on copper*. Electrochimica Acta **46** (2001) 2337 – 2342.

[51] SCHWAB, K., HENRIKSEN, E., WORLOCK, J., AND ROUKES, M., *Measurement of the quantum of thermal conductance*. Nature **404** (2000) 974–7.

[52] CROSS, M. AND LIFSHITZ, R., *Elastic wave transmission at an abrupt junction in a thin plate with application to heat transport and vibrations in mesoscopic systems*. Physical Review B **64** (2001) 085324.

[53] CHANG, C.-M. AND GELLER, M., *Mesoscopic phonon transmission through a nanowire-bulk contact*. Physical Review B **71** (2005) 125304.

[54] HEKKING, F., NISKANEN, A., AND PEKOLA, J., *Electron-phonon coupling and longitudinal mechanical-mode cooling in a metallic nanowire*. Physical Review B **77** (2008) 033401.

[55] ROUKES, M., FREEMAN, M., GERMAIN, R., AND RICHARDSON, R., *Hot electrons and energy transport in metals at millikelvin temperatures*. Physical Review (1985) 422–425.

[56] KOPPINEN, P. AND MAASILTA, I., *Cooling of suspended nanostructures with tunnel junctions*. Journal of Physics: Conference Series **150** (2009) 012025.

[57] KOPPINEN, P. J., ISOTALO, T. J., AND MAASILTA, I. J., *Boundary engineering for sinis bolometers with integrated tunnel junction coolers*. AIP Conference Proceedings **318** (2009) 318–321.